Insights into sulfur cycling at subduction zones from *in-situ* isotopic analysis of sulfides in high-pressure serpentinites and 'hybrid' samples from Alpine Corsica

R.J. Crossley[1, 2*], K.A. Evans[1], H. Jeon[3, 4] & M.R. Kilburn[3]

[1]School of Earth and Planetary Sciences, Curtin University, GPO Box U1987, Perth, WA 6845, Australia.

[2]Present address: School of Geosciences, University of the Witwatersrand, Private Bag 3, 2050 Wits, Johannesburg, South Africa.

[3]Centre for Microscopy, Characterisation and Analysis, University of Western Australia, Crawley, WA 6009, Australia.

[4]Present address: Department of Geosciences, Swedish Museum of Natural History, Box 50 007, SE-10405 Stockholm, Sweden.

*corresponding author: Rosalind.Crossley@wits.ac.za

Keywords

Sulfur; Subduction; Stable isotope; In-situ; Serpentinite; Redox

Abstract

Devolatilisation of serpentinites at depth in subduction zones contributes significant quantities of sulfur and other redox sensitive elements to the sub-arc mantle. However, the fate of sulfur in subducted serpentinites is poorly constrained. Textures of sulfur-bearing phases in subducted serpentinites are rarely studied, yet provide important information on the changes to sulfur distribution throughout the subduction cycle and as a result of fluid infiltration. $\delta^{34}S$ values of sulfides provide constraints on sulfur sources, the redox state of sulfur in the host mineral, and on processes that have occurred subsequent to sulfide crystallisation, including interaction with oxidised or reduced fluids. Therefore, it is possible to use $\delta^{34}S$ values in subducted serpentinites to constrain the redox state of sulfur in sulfides and subduction zone fluids. Furthermore, the proximity of serpentinites to ocean crust and metasediments may influence enrichment or depletion of ^{34}S during subduction relative to serpentinites distal to such lithologies.

This study investigates the redox state, the likelihood of sulfur addition to the sub-arc mantle from serpentinite dehydration, and the distribution of sulfur within subducted serpentinites and 'hybrid' mafic/ultramafic rocks from Alpine Corsica. The techniques utilised include petrographic analysis, *in-situ* sulfur isotopic analysis and trace element analysis of sulfides hosted in these rocks. All sulfides investigated have high $\delta^{34}S$ values of 1.9–15.5‰, which suggests that mantle-derived sulfur ($\delta^{34}S \sim 0.1$‰), was not the sole source of sulfur. The highest $\delta^{34}S$ values are recorded in pyrites of a hybrid mafic/ultramafic sample. High $\delta^{34}S$ values are preserved in sulfides attributed to prograde metamorphism, and is most consistent with the retention of sulfur derived from hydrothermal sulfate reduction on the seafloor. However, a shift towards higher $\delta^{34}S$ values in sulfides associated with the advanced stages of exhumation suggests that late stage exhumation enables enhanced access to slab-derived fluids bearing oxidised sulfur (SO_4^{2-} or SO_2). Such fluids may have been derived from the devolatilisation of serpentinite at greater depth, or from other lithologies.

1. Introduction

Sulfur is subducted in variable oxidation states from sulfate (+6) to sulfide (-2) within altered ocean crust, hydrated mantle lithosphere and ocean floor sediments, to contribute a significant flux of redox budget to subduction zones (Evans, 2006; Evans, 2012). Sulfur input

to subduction zones is an order of magnitude higher than the flux of sulfur released (Evans, 2012; Evans et al., 2014). However, changes to the oxidation state of sulfur, the processes that sulfur undergoes during subduction and the quantity of sulfur transferred to the sub-arc mantle and deep mantle are poorly constrained (e.g., Evans et al., 2014). The redox state and the concentration of sulfur in the sub-arc mantle are of particular importance because genetic models for arc-related ore deposits currently require an oxidised sub-arc mantle (e.g., Mungall et al., 2002).

The combined approach of sulfide mineral paragenesis and *in-situ* measurement of sulfur isotopes ($\delta^{34}S$) in sulfur-bearing mineral phases within rocks that have undergone subduction and, at a later stage, exhumation, can be used to constrain the source, redox state and processes that sulfur has undergone throughout the subduction cycle. Such processes include bacterial sulfate reduction, fluid infiltration or devolatilisation. ^{34}S partitions preferentially into oxidised species relative to ^{32}S; for example, present day seawater sulfate has a $\delta^{34}S$ value of ~20–21‰ (Rees, 1978; Paytan et al., 1998, 2004; Tostevin et al. 2014), whereas mantle sulfur is 0.1±0.5‰ (Sakai et al., 1984; Shanks et al., 1995; Alt and Shanks, 1998). The observation that porphyry arc-related ore deposits have $\delta^{34}S$ values up to ~13‰ higher than the mantle (Alt et al., 1993; Ishihara & Sasaki, 1989), requires a source of ^{34}S, which is proposed to have originated via sulfate transfer from the slab (Richards, 2015). Pre-subduction fixation of sulfate in serpentinised mantle lithosphere, oceanic crust and sediments is considered to account for sulfate enrichment in the slab (Ishihara and Sasaki, 1989; Shanks et al., 1981; Wallace & Edmonds, 2011; Alt et al., 2012a; Debret et al., 2014; Evans et al., 2014). However, sulfur release and retention within the slab during subduction, and the mechanisms that control the distribution of sulfur are not well understood.

Attempts have been made to constrain subduction-related fluxes of sulfur from the oceanic crust (Evans et al., 2014; Marschall & Shimizu, 2012; Aulbach et al., 2012), but fluxes from the hydrated mantle lithosphere during subduction are rarely investigated, with some exceptions (e.g., Alt et al., 2012a; Alt et al., 2012b; Shimizu et al., 2013). The hydrated mantle lithosphere component of the slab is of particular interest because its dehydration at depth within the subduction channel has the potential to release a significant volume of fluids, which could migrate to the sub-arc mantle. Various processes can affect the sulfur isotope composition of peridotite exhumed on the seafloor at spreading centres, including microbial sulfate reduction (Alt and Shanks, 1998; Alt et al., 2007; Schwarzenbach et al., 2012; Ono et al., 2012) and hydrothermal sulfate reduction (Alt and Shanks, 2003; Bach et

al., 2004, Alt et al., 2007, Delacour et al., 2008; Peters et al., 2010, Ono et al., 2012). Temperature governs the process that prevails on the seafloor (e.g., Schwarzenbach et al., 2018). A contribution from seawater-derived sulfate in modern day can result in ^{34}S-enriched serpentinites with δ^{34}S values of up to ~20‰ compared to the Earth's mantle (Delacour et al., 2008; Alt & Shanks, 2003; Alt et al., 2012a, Tostevin et al., 2014). Therefore, upon subduction, serpentinites may carry oxidised sulfur to the sub-arc mantle or deep mantle. In contrast, microbial sulfate reduction on the seafloor at low temperature results in a ^{34}S depleted reservoir of reduced sulfur, and resultant δ^{34}S values as low as -34‰ (Alt and Shanks, 1998; Schwarzenbach et al. 2012). Therefore, the oxidation state of sulfur input into subduction zones is strongly dependent on temperature, whether the system is open or closed with respect to sulfur, and whether microbial or hydrothermal processes govern sulfate reduction.

Δ^{33}S is used to describe the extent of mass independent fractionation (MIF); the degree to which variations in isotope abundance are not dependent on mass. Δ^{33}S values provide additional information compared to the measurement of δ^{34}S values alone (Ono et al., 2012; Schwarzenbach et al., 2018), and allows distinction between open and closed system sulfate reduction, and between bacterial sulfate reduction and hydrothermal sulfate reduction that can be traced through subduction. Non-zero MIF values for sulfur indicate that the analysed sulfur deviates from the terrestrial line defined by the slope of a fractionation line between δ^{34}S and δ^{33}S for the Earth-Moon system, where the slope is 0.515 (Seal, 2006 and references therein). Modern day seawater sulfate has a Δ^{33}S value of 0.050±0.0003‰ (Ono et al., 2012), whereas mid ocean ridge basalts (MORB) from the East Pacific Rise have Δ^{33}S values within error of zero at ~0.001±0.017‰ (Ono et al., 2012). A study of samples from the Iberian Margin basement revealed that serpentinised peridotites have higher Δ^{33}S values than basaltic samples with values ranging from 0.00 to 0.16 in peridotites (Ono et al., 2012; Schwarzenbach et al., 2018), compared to -0.06 to 0.04 in the basalts (Ono et al., 2012). Lower Δ^{33}S values (-0.06 to 0.02) have been reported for Northern Appenine serpentinites (Schwarzenbach et al., 2018), and similarly low Δ^{33}S values (-0.01 to 0.01) are reported for basalts from the Pacific-Antarctic ridge, however, these values are indistinguishable from the Canyon Diablo Troilite international standard (Labidi et al., 2014).

The proximity of serpentinites to ocean crust and metasediments in the subduction channel may influence the redox state and concentration of sulfur in both serpentinites and other lithologies, and therefore the sulfur isotope compositions, either through the loss of

oxidised or reduced fluids from serpentinites, or the infiltration of fluids from other lithologies. For example, seafloor serpentinites associated with gabbroic intrusions have been shown to have higher $\delta^{34}S$ values than serpentinites elsewhere (Alt and Shanks, 2003). Mixing of sediments/oceanic crust and mantle along the slab/sub-arc mantle interface at high-pressure produces 'hybrid' rocks, which are physical or chemical mixtures of two or more end member rock types, such as sediment, peridotite (mantle), gabbro and basalt (Spandler and Pirard, 2013; Marschall and Schumacher, 2012), and have chemical and isotopic compositions that reflect this mixing. Hybrid rocks have been recognised as important carriers of volatile elements to even greater depths than the serpentinised mantle (e.g., Spandler et al. 2008), and could play an essential role in the transfer of sulfur to the sub-arc mantle.

Although whole rock $\delta^{34}S$ data are available for subducted ultramafic rocks (Alt et al., 2012a; b), subducted ultramafic rocks undergo several stages of alteration starting at the seafloor, followed by subduction and exhumation, such that whole rock sulfur isotope analysis provides a record of superimposed processes. *In-situ* $\delta^{34}S$ measurements of sulfides with well-constrained parageneses provide an opportunity to sample the evolution of sulfur throughout the metamorphic evolution of the samples. To the authors' best knowledge the only other published *in-situ* $\delta^{34}S$ values for subducted ultramafic rocks are reported in two conference abstracts, Santiago-Ramos et al. (2012) and Shimizu et al. (2013) who measured $\delta^{34}S$ values of pentlandite and heazlewoodite grains within Erro Tobbio serpentinites. These studies report relatively low $\delta^{34}S$ values for sulfide grains within low temperature serpentinites (-3.2 to 5.9‰), and variable $\delta^{34}S$ values from -1.1 to 18.3‰ for sulfide grains within subducted serpentinites.

In this study, redox conditions, the likelihood of sulfur transfer to the sub-arc mantle from serpentinite dehydration, and the distribution of sulfur within subducted serpentinites and hybrid mafic/ultramafic rocks are investigated through a combination of petrographic analysis, *in-situ* sulfur isotope and trace element analyses of sulfides hosted in these rocks.

2. Geological Background

Thirty samples were collected from the Schistes Lustrés complex at the two localities Serra di Pigno and Capu Corvoli, Cap Corse (Fig. 1). Serra di Pigno lies approximately 10 km west of Bastia, on Cap Corse (Fig. 1a). The sample collection includes metagabbros, metasediments, serpentinites and hybrid rocks from the Schistes Lustrés complex.

Serpentinite samples from Serra di Pigno were collected adjacent to metasediments, metagabbros and metabasalts, and distal to these lithologies (Fig. 1b, c). Hybrid samples from Capu Corvoli were collected from slivers next to metagabbro and <0.5 km from calcareous schist (Fig. 1d, e). These localities were chosen because they allow the assessment of lithological controls on the isotopic composition of sulfur.

During the Middle to Late Jurassic, the ophiolites and associated sediments were considered to have been part of an ocean-continent transition (OCT) zone (e.g., Vitale Brovarone and Herwartz, 2013; Vitale Brovarone et al., 2013; Magott et al., 2016). At this time, seawater sulfate had $\delta^{34}S$ values of ~ 17‰ (Kampschulte and Strauss, 2004). Field observations consistent with an OCT setting of the ophiolites prior to subduction include the juxtaposition of continental slices and ultramafic rocks, ultramafic clasts within carbonaceous sediments, the presence of ophicalcites, and variable interlayering of sediments with mafic and ultramafic lithologies at Serra di Pigno (Meresse et al., 2012) and other localities within Alpine Corsica (Vitale Brovarone et al., 2011).

The samples from the Serra di Pigno region record blueschist to eclogite facies metamorphism and underwent high-pressure metamorphism from ~55 to 34 Ma (Ravna et al., 2010; Vitale Brovarone et al. 2011, Vitale Brovarone and Herwartz, 2013). The minimum pressure recorded during subduction is estimated to be ~1.3–2.6 GPa (Lahondère and Guerrot, 1997; Vitale Brovarone et al., 2013), and on the basis of Raman spectroscopy of carbonaceous material (Vitale Brovarone et al., 2013), the peak metamorphic temperature is constrained to ~414–471ºC.

The chlorite schist and talc schist hybrid mafic/ultramafic samples were collected at Capu Corvoli, Cap Corse. The samples are from a shear zone with a top-to-the-west to northwest sense of shear, parallel to a series of proximal WNW to NW shallowly dipping thrust faults, which were previously interpreted to divide the lawsonite-blueschist Upper Castagniccia metasediments and lawsonite-eclogite ophiolites (Lahondère, 1992). The sense of shear is uniform with deformation associated with prograde metamorphism (Mattauer et al., 1977; 1981; Faure and Malavielle, 1981; Harris, 1985; Warburton, 1986; Magott et al., 2016). Within the shear zone, slivers of the hybrid lithologies are juxtaposed with metagabbro. Recent P-T estimates suggest that the Upper Castagniccia metasediments record eclogite facies metamorphism (Vitale Brovarone et al., 2013 & references therein). Thus, the Capu Corvoli samples record similar or higher P-T conditions than the Serra di Pigno

samples at ~490–550 °C and 1.9–2.6 GPa (Ravna et al., 2010; Vitale Brovarone et al., 2011; 2013).

In this study, existing estimates of P-T conditions (e.g., Agard and Vitale-Brovarone, 2013), detailed sample petrography and mineral chemistry are used to distinguish between sulfides associated with mantle, seafloor, prograde, peak and retrograde stages. In the seafloor environment, sulfur is present as mantle sulfides, or as sulfides derived from seawater sulfate and precipitated during hydrothermal alteration. Such sulfides could be preserved during prograde metamorphism, or these sulfides may recrystallize at this stage. The onset of exhumation is marked by a decrease in pressure (Agard and Vitale-Brovarone, 2013). At this stage, maximum temperatures are recorded, such that heating via continued thermal equilibration is still occurring at the onset of exhumation. Additionally, it is likely that the rocks remain partially hydrated even after they have undergone prograde metamorphism, therefore, therefore fluids are also released at the onset of exhumation (e.g., Miller and Cartwright, 2006). Hence, the rocks may have access to both prograde and exhumation-related fluids during this stage. Retrogressed sulfides associated with such fluids provide insight into the composition of fluids released from the slab.

3. Petrography

Different sulfide generations are attributed to stages of metamorphism on the basis of their textural association with silicate minerals, where silicate mineral stability has been well constrained at a range of temperatures and pressures. Primary sulfides are typically polyhedral blebs with concave inward boundaries (Seyler et al., 2007; Schwarzenbach et al., 2012), a textural characteristic that is not observed in any of the samples. In this section, the numbering 1-3 is used to assign sulfides to stability during (1) prograde metamorphism (2) the onset of exhumation, and (3) advanced stages of exhumation.

3.1 Serra di Pigno

3.1.1 Serpentinite CO13-40

CO13-40 is a serpentinite sample distal to other lithologies (grid reference: WGS 84, zone 32T, 0533122 mE 4728302 mN, Fig. 1 a, b). Pentlandite1 (pn1) consist of grains up to ~50 µm in diameter associated with magnetite. Both magnetite and pn1 overprint the foliation defined by fine-grained antigorite (atg1), and contain inclusions of atg1 (Fig. 2a). Orientated and foliated antigorite (atg1) has a fine and interlocking texture consistent with prograde

growth (e.g., Li et al., 2004), and defines the dominant foliation. Given the inclusion of atg1 in pn1, it is inferred that pn1 maintained stability during prograde to peak metamorphism. A late generation of antigorite (atg2) cuts pn1 (Fig. 2a) and therefore further constrains pn1 growth to a stage prior to retrogression.

3.1.2 Serpentinite CO13-33

CO13-33 is a serpentinite sample collected from an outcrop proximal to metagabbro and metaquartzite (grid reference: WGS 84, zone 32T 0533514 mE 4729532 mN, Fig. 1a, b). Early pentlandite (pn1; Fig. 2b) occurs as elongate grains (~5 μm) associated with heazlewoodite, magnetite1, kamacite (~5 μm), fine matrix antigorite and fine balangeroite veins (<5 μm across). Balangeroite growth has previously been ascribed to prograde metamorphism within the antigorite stability field in both the Piemonte zone in the Alps (Groppo and Compagnoni, 2007), and Sasaguri, Japan (Evans and Kuehner, 2011). The association of pn1 with fine-grained antigorite (atg1) and balangeroite implies that pn1 was stable during prograde metamorphism. Chlorite growth is associated with antigorite dehydration (e.g., Padrón-Navarta et al., 2013; Scambelluri et al., 2014; Evans and Powell, 2015), overprinting atg1. Pentlandite2 partially replaces chlorite (pn2; Fig 2c) and contains inclusions of atg1. Therefore, pn2 postdates prograde–peak metamorphism and is considered to have grown at the onset of exhumation, overprinted by a later generation of magnetite at the rim. A late phase of pentlandite, pn3, occurs as euhedral to subhedral grains that overprint a late generation of antigorite veins, and is synchronous with or includes late magnetite (Fig. 2d), thus pn3 is related to advanced stages of exhumation.

3.1.3 Serpentinite CO13-55

CO13-55 is a serpentinite sample proximal to metagabbro and calcareous schist (grid reference: WGS 84, zone 32T, 0533398 mE 4729368 mN, Fig. 1a, b). Primary phases are absent; all spinel grains are ‘porous’, Al-poor, Cr-Fe spinel with mt1 rims, which are compositionally and texturally consistent with alteration of primary spinel during seafloor and/or prograde metamorphism (Evans and Frost, 1975; Bliss and MacLean, 1975; Wylie et al., 1987; Kimball, 1990; Frost, 1991; Barnes, 2000; Mellini et al., 2005; Merlini et al., 2009; Mukherjee et al., 2010; Grieco and Merlini, 2012; Gervilla et al., 2012; Colás et al., 2014). Phases stable during prograde to peak metamorphism include fine-grained antigorite (atg1), which comprises the matrix (<1 to 5 μm), chlorite, pentlandite1 (pn1), pyrite and chalcopyrite. Altered porous spinels contain inclusions of fine-grained antigorite (atg1) and

pentlandite (pn1), consistent with the interpretation of recrystallisation of antigorite from precursor lizardite and retention of pn1 during prograde metamorphism. Pentlandite1 also consists of larger grains (10–30 μm), which contain small Cr-Fe spinel grains (2–3 μm) and overprints or is in equilibrium with mt1 but is itself cut by atg2 veins (Fig. 2e). Phases associated with the onset of exhumation include pentlandite2 (pn2) and mt2. Pentlandite2 and mt2 are associated with diopside, although some grains of diopside are observed overprinting these phases. Diopside growth is constrained to the onset of exhumation, or after, because it overprints prograde antigorite and peak chlorite. Additionally, diopside is comprised of randomly orientated idioblastic prims (Fig. 2f, g) consistent with retrograde textures previously described elsewhere (Groppo and Compagnoni, 2007). Pentlandite3 is synchronous with or occurs as rims on late antigorite cross-cutting veins (Fig. 2h) and therefore pn3 postdates the veins (Fig. 2h), where antigorite veins cut prograde to peak phases (pyrite, chalcopyrite, pn1 and mt1) (Fig. 2e), and phases associated with the onset of exhumation (pn2 and mt2).

3.2 Capu Corvoli

3.2.1 Chlorite schist CO14-03

CO14-03 is a chlorite schist in contact with metagabbro that lies structurally above the sample (grid reference: WGS 84, zone 32T, 0529140 mE 4753069 mN; Fig. 1d, e). There is little evidence for the retention of primary or seafloor phases. The earliest phases associated with prograde to peak metamorphism are thin (<5 μm), orientated laths of foliated chlorite and antigorite, which together comprise the matrix. Magnetite is constrained to the onset of exhumation because it cuts the prograde to peak antigorite-chlorite defined foliation. Magnetite has undergone brittle deformation and is cut by second generation of chlorite (chl2) veins, and overprinted by titanite, a low-pressure Ti-rich phase (e.g., Laird & Albee, 1981; Spear, 1981; Ernst & Liu, 1998). Thus, magnetite growth is constrained to the earliest stages of exhumation. Pyrite occurs as euhedral aggregates isolated in the matrix, as rims on magnetite or within fractures connected to the matrix in magnetite (Fig. 2i, j). Pyrite is enclosed by titanite, although some grains contain inclusions of titanite towards the rim implying synchronous pyrite and titanite growth for some time. Pyrite is therefore attributed to lower pressures associated with an advanced stage of exhumation, and is thus referred to as py3.

3.2.2 Talc schist CO14-04

CO14-04 is a talc schist sample in contact with metagabbro associated with CO14-03 structurally below the sample (grid reference: WGS 84, zone 32T, 0529107 mE 4753071 mN, Fig. 1d, e). Primary or seafloor phases consist of an early generation of pyrrhotite (po0 <5 μm), Cr-rich spinel cores to magnetite, and Pt-rich alloys (rare, ~2 μm). Cr-Al spinels are proposed to be primary based on their Al-rich composition (e.g. Barnes and Roeder, 2001), although the grains could have undergone alteration during seafloor alteration from more Mg-rich primary compositions. The association of spinel with pyrrhotite0 and Pt-rich alloys attributes these phases to primary growth and possible alteration during seafloor processes. Prograde phases include pyrite (py1), an early generation of talc (talc1), magnetite, a later generation of pyrrhotite (po1) and chlorite. Talc1 growth is attributed to metasomatism during subduction (e.g., Spandler et al., 2008). Pyrite1 contains inclusions of pyrrhotite0, Cr-Al spinel and a Pt-rich alloy. Given the inclusion of Cr-spinel in py1, and magnetite rims on Cr-rich spinel, py1 and magnetite growth are synchronous. Chlorite, which is attributed to peak metamorphism, cross-cuts magnetite, thus the growth of magnetite and py1 predate peak metamorphism. Pyrrhotite1 is texturally later than py1, given its inclusion in rims on py1, though possible incorporation from the matrix cannot be excluded. A second generation of pyrite (py2) cuts the prograde talc1 matrix and peak metamorphic chlorite, and has coarse talc2 rims (Fig. 2i). Talc stability is restricted to pressures below 1.5 GPa (Evans & Powell, 2015), therefore the talc rim records decompression associated with advanced stages of exhumation (e.g., Crossley et al., 2017). Pyrite2 is therefore constrained to growth during the onset of exhumation.

4. Methods

The samples selected for this study contain sulfides of suitable size for secondary ion mass spectrometry (SIMS) analysis, using a large geometry (LG) SIMS, a Cameca IMS 1280, and NanoSIMS. Prior to *in-situ* analysis, detailed petrographic analysis was undertaken using transmitted and reflected light microscopy, and scanning electron microscopy (SEM) and energy dispersive spectrometry (EDS). Electron probe microanalysis (EPMA) was performed prior to SIMS analysis to determine compositions of sulfides. In addition, EPMA and NanoSIMS mapping were employed to search for any discrete zoning in sulfide minerals.

4.1 Sample Preparation

Prior to SIMS and NanoSIMS analysis, representative areas were selected from thin section billets, where billets were cut perpendicular to sample foliation, and drilled from each sample using a hollow cylindrical diamond coated drill bit that produces 7 mm pucks. The pucks were mounted in 25 mm diameter epoxy disks, polished and coated with ~30 nm of Au to provide electrical conductivity at high voltage and thus prevent sample charging. Using a precision saw, the mounts were trimmed by approximately one third to allow a reusable standard piece that contains Sierra pyrite and VMSO pentlandite standards to be mounted alongside the unknown samples in the ion probe.

4.2 EPMA Mapping

Trace element mapping was carried out on sulfide grains selected for SIMS analysis using the JEOL 8530F Hyperprobe at the Centre for Microscopy, Characterisation and Analysis (CMCA) at the University of Western Australia (UWA). The carbon coating was 25 nm in thickness. Wavelength dispersive spectrometry (WDS) operating conditions included a 20 kV accelerating voltage, a 20 nA beam current, and a 40s dwell time. Mean atomic number (MAN) background corrections were used with a total on-peak counting time of 20 s per element. The standards used for calibration include Ni, Co, Pyrite (S) and ASP200 (arsenopyrite; As). WDS was conducted using the crystals PETJ for S Kα, TAP for As Lα, and LiF for Fe Kα. The use of two crystals, LiFH and LiF, enabled optimum detection of Co Kα and Ni Kα. Data reduction was performed using the Probe for EPMA software (Donovan et al., 2012), and quantitative element maps were generated from WDS X-ray intensity maps using the CalcImage and Surfer 10.2 software. A matrix correction was conducted at each pixel and a script file was output for each element. Element concentrations were calculated using the mean atomic number (MAN) background method, where after background correction, X-ray intensity was multiplied by the matrix effect correction factors Z (atomic number correction; Duncumb and Reed, 1968), A (absorption correction; Philibert, 1963; Duncumb & Shields; 1966; Heinrich, 1969; Bearden, 1964; Heinrich, 1986) and F (characteristic fluorescence correction; Reed, 1965), relative to standards. The script files generated by CalcImage were input into Surfer 10.2 to plot maps for each element.

Point analyses were carried out under the same operating conditions but additional standards were used for calibration including wollastonite (Si), San Carlos Olivine (Mg), Crocoite (Pb), ZnO, Cu, Mn, Cr_2O_3, Bi_2Se_3, Ag, GaAs (As), and Sb. In addition, WDS was

conducted using the crystals LiF for Ni Kα and Co Kα, TAP for Si Kα, Mg Kα and Se Lα, PETJ (Pb mα), LiFH (Zn Kα, Cu Kα, Mn Kα, Cr Kα), PETJ (Ag Lα and Bi Mα) and LiF (Sb Lα).

4.3 Secondary Ion Mass Spectrometry

4.3.1 NanoSIMS

Mapping of small pentlandite grains in sample CO13-40 was performed on the CAMECA NanoSIMS N50 at the CMCA, UWA, prior to LG-SIMS analysis. Secondary ion images were acquired using a focused Cs^+ primary ion beam, with a nominal beam diameter of ~100 nm. Electron multipliers at the five detector sites were positioned to detect the secondary ions FeS^-, CoS^-, NiS^-, CuS^-, AsS^-, Te^- and Au^- on masses 88, 91, 92, 97, 107, 130 and 197, respectively. The mass spectrometer was tuned using a 30 μm entrance slit, and peak positions were calibrated using sulfide minerals and metallic Au. Areas of 60 × 60 μm and 30 × 30 μm were imaged at a pixel resolution of 512 × 512, with a primary beam current of approximately 2.8 pA, and a dwell time of 25 ms/pixel. Smaller areas of 15 × 15 μm were imaged at a pixel resolution of 256 × 256, with a primary beam current of approximately 1.2 pA and a dwell time of 45 ms/pixel. All areas were pre-sputtered to 10^{17} Cs ions/cm^2 prior to imaging. All images were corrected for 44 ns detector deadtime and processed using the NRIMS plugin for ImageJ (http://nrims.harvard.edu/software).

4.3.2 LG-SIMS: Cameca IMS 1280

4.3.2.1 Standards

Sierra pyrite (fragments from the same pyrite block have been previously reported as Sonora-3) is from a 9 kg cube of pyrite from a Cretaceous porphyry copper mine in Sonora, Mexico, described in Wacey et al. (2011), Farquhar et al. (2013) and Evans et al. (2014). VMSO pentlandite is sourced from a massive sulfide lens from the Ni-Cu-PGE Long-Victor mine, Kambalda, Western Australia metamorphosed to amphibolite facies (Barnes et al., 2013, and references therein). All $\delta^{34}S$ values in this study are relative to Vienna Canyon Diablo Troilite (VCDT), the value of which is assumed to be 0.0450045 (Ault and Jensen, 1963). The details of bulk $\delta^{34}S$ measurement by laser fluorination, heterogeneity, precision and reproducibility of the Sierra pyrite and VMSO pentlandite standards are discussed in detail in LaFlamme et al. (2016). Both Sierra and VMSO are of similar major element (Fe, Ni, Co and S) compositions to the pyrites and pentlandites studied here (section 5.1).

4.3.2.2 Method

Ion microprobe analysis was carried out on the CAMECA IMS 1280 at the CMCA, UWA, to measure *in-situ* sulfur isotope compositions ($^{33}S/^{32}S$ and $^{34}S/^{32}S$). A ca. 2–3 nA focused Cs^+ primary beam was operated at 10 kV and the secondary ion beam was extracted at -10 kV. The analysis area was presputtered using a 25 × 25 μm (or 20 × 20 μm for pentlandite) raster for 30 seconds (or 10 sec for pentlandite; see below) followed by automated secondary centering in the field aperture (FA; 4000 μm) and entrance slit (ES; 60 μm). The analysis used a 15 × 15 μm (or 10 × 10 μm for pentlandite) raster employing dynamic transfer at a 133 × field magnification for 45 × 4 second integrations. Three sulfur isotopes were measured simultaneously using three Faraday Cup detectors with amplifiers of 10^{10} Ω resistor for ^{32}S and 10^{11} Ω for ^{33}S and ^{34}S. An exit slit of 500 μm was used on each of the multicollector detectors, providing a nominal mass resolving power (MRP) of ca. 2500. As this MRP does not allow for complete resolution of the ^{32}S ^{1}H and ^{33}S peaks, the detector collecting ^{33}S was offset to the low mass side, sufficient to exclude tailing of the ^{32}S ^{1}H signal (e.g., LaFlamme et al., 2016). The magnetic field was regulated using nuclear magnetic resonance (NMR). To avoid any problems related to non-conducting inclusions and/or to the very small pentlandite grains in the silicate matrix, a normal incidence electron gun was used for charge compensation in all analyses. Although ^{36}S was not analysed, an electron multiplier detector was also setup to locate pentlandite grains <20 μm using the ^{36}S ion image. For these pentlandite analyses, the areas were pre-burnt to see their ion images so the presputter time was reduced to 10 seconds. Measurements of an appropriate standard after each block of four to five analyses allowed the assessment of instrumental drift. The method for data reduction is described in Appendix A.

Incorporation of minute antigorite inclusions in the analysis volume (<2 μm) may have affected S isotope ratios via the changes to matrix fractionation effects, however the inclusions would not contain sufficient sulfur to alter $\delta^{34}S$ values. Sulfide grains were checked carefully for such inclusions using SEM and nominally inclusion-free areas were analysed. After the measurements were finished, the analysed spots were checked again using SEM.

5. Results

5.1 Sulfide mineral compositions

Average major element concentrations for sulfides are provided in Table 1. The full dataset is provided in Appendix B. Formulae of sulfide minerals were calculated using charge balance and stoichiometric constraints. Different generations of sulfides are indistinguishable on the basis of mineral composition. The average mineral formulae for pentlandite in CO13-33 and CO13-55 is $Fe_{3.5–3.9}Ni_{4.8–5.2}Co_{0.3}S_8$ (*n* = 36 and 30, respectively). Pentlandite in CO13-40 has higher concentrations of Fe and contains lower concentrations of Ni and slightly lower Co concentrations with the average formula $Fe_{4–4.2}Ni_{4.6–4.8}Co_{0.2–0.3}S_8$. Pyrites in CO14-03 and CO14-04 are stoichiometric (FeS_2) with minor (up to 0.01 cations) Co and Ni replacing Fe per formula unit in each sample.

5.2 Sulfur isotope compositions and trace element mapping

Here the results are presented as $\delta^{34}S$ values, non-zero $\Delta^{33}S$ values, and EPMA trace element maps. The complete sulfur isotope data set including the $\delta^{33}S$ values and measured standard sulfur isotope compositions are provided in Appendix C. All uncertainties reported in the text, figures and tables are 2σ, unless otherwise noted.

5.2.1 Serra di Pigno

5.2.1.1 Distal Serpentinite CO13-40

$\delta^{34}S$ values in CO13-40 pentlandite range from 4.3 to 10.4‰ (n=30) (Fig. 3a, Fig. 4a–e, Table 2, Appendix C). Three analyses have non-zero $\Delta^{33}S$ values of 0.52±0.30‰ (a3_s12-3), 0.67±0.50‰ (a3_s1-2) and 0.38±0.24 ‰ (a3_s3) (Table 3). Trace element NanoSIMS maps reveal zonation in Cu, Co, As and Ni. Co, As and Ni zoning is decoupled from the Cu zoning (Fig. 4f). Due to the small size of the grains (up to 50 μm), it was not possible to determine the relationship of the zonation to the $\delta^{34}S$ ratios, therefore homogeneous areas were chosen for analysis.

5.2.1.2 Serpentinite proximal to metaquartzite and metagabbro CO13-33

$\delta^{34}S$ values in pentlandite in CO13-33 range from 1.8 to 9.2 ‰ (n = 18) (Table 2, Appendix C; Fig. 3b; Fig. 5a–e). The sulfides analysed include pn1 (n=9; Fig. 5a, b), pn2 (n=9; Fig. 5b, c) and pn3 (n=5; Fig. 5d–e). The histograms display a unimodal distribution (Fig 3b) and Mann-Whitney U tests (Appendix D) do not reveal significant variation in $\delta^{34}S$ between the different generations of pentlandite from early to late grains. Pn1 grains have

similar $\delta^{34}S$ values to pn2 grains with values of 6.5 to 8.8‰ in pn1 grains, compared to 5.5 to 8.3‰ in pn2 grains ($p = 0.79$), where p indicates the probability that the pn1 and pn2 analyses are from the same distribution. $\delta^{34}S$ values of pn3 grains vary from 1.8–8.4‰, and are not significantly different from pn1 and pn2 ($p = 0.39$). EPMA mapping reveals homogenous Co concentrations in the interior of pn2, but higher Co concentrations towards pn2 rims, (Fig. 5f).

5.2.1.3 Serpentinite proximal to calcareous-schist and metagabbro (CO13-55)

$\delta^{34}S$ values in pentlandite within CO13-55 range from 1.9 to 8.0‰ (n=19; Table 2, Appendix C, Fig. 3c); pn1 from 1.9 to 5.7‰ (n=10; Fig. 6a–c), pn2 $\delta^{34}S$ from 3.1–6.9‰ (n=5; Fig. 6d) and pn3 from 5.5–8.0‰ (n=5; Fig. 6e–f). The Mann Whitney U test revealed a significant difference between pn1 and pn3 at a level of significance of 1% (p = 0.0078), but not between pn2 and pn3 (p = 0.05). Four analyses have non-zero $\Delta^{33}S$ values of 0.33±0.23‰ (area2_s1-1, pn1), 0.37±0.28‰ (area2_s3-1; pn2), 0.38±0.23‰ (area3_s2-1, pn3) and 0.49±0.31‰ (Table 3, pn1). Zonation in Co is not evident in CO13-55 pentlandites (Fig. 6b).

5.2.2 Capu Corvoli

5.2.2.1 Chlorite Schist CO14-03

Relative to other samples in this study, CO14-03 pyrite $\delta^{34}S$ values are very heterogeneous, within individual pyrite grains and between different pyrite grains, with values ranging from 5.9 to 15.5 ‰ (n=32; Table 2, Appendix C, Fig. 3d). The majority of grains have $\delta^{34}S$ values from 6–9‰ (n = 21), with higher $\delta^{34}S$ values from 10.8–15.5 ‰ (n = 11). Some pyrites appear to form clusters, while others are isolated in the matrix. Although no differences in relative timing are inferred from textural analysis, isolated pyrites (Fig. 7 a–c, n=17) were compared to pyrites in clusters (Fig. 7d–e, n=15). Significantly higher $\delta^{34}S$ values were recorded in pyrite that formed clusters (p = 0.0057). EMPA mapping reveals fine scaled zonation of Co from 0.1 to 1.2 wt%, and of Ni from 0.1 to 0.4 wt% (Fig. 8a–c). The Co and Ni zonation does not show a significant correlation with $\delta^{34}S$ (R^2 = 0.3 and 0.23, respectively, Fig. 8d).

5.2.2.2 Talc Schist CO14-04

CO14-04 pyrites appear to be relatively homogeneous with $\delta^{34}S$ values of 3.6–5.4‰ (n=49). Py1 has slightly higher values (4.1–5.4‰, n=12; Fig. 9a–d), compared to py2 which has a larger range from 3.1–5.0‰ (n=37; Fig. 9e–f), where there is a low probability of both pyrite generations sampling the same isotopic population (p=0.0065). Additionally, three

$\Delta^{33}S$ values are significantly different to zero, s1 in area 1 (0.11±0.10‰), s1 analysis 9 in area 2 (-0.16±0.12‰) and S1 in area 3 (-0.17±0.15‰).

EPMA maps show Co and Ni zonation at a finer scale than the interaction volume of SIMS analysis (Fig. 8d–f). Mann-Whitney U test calculations (Appendix D) revealed that the correlation between Co and $\delta^{34}S$ is significant at a 5% level of significance (P=0.048, R^2=0.49; Fig. 8g) but Ni is decoupled from $\delta^{34}S$ (R^2=0.12, Fig. 8h).

6. Discussion

Primary, seafloor and prograde sulfides provide an insight on the inputs of sulfur to subduction zones, while sulfides associated with the onset of exhumation, provide a record of fluid composition released from the slab. Primary sulfide grains occur as polyhedral blebs with concave inward boundaries (Seyler et al., 2007; Schwarzenbach et al., 2012), a textural characteristic not observed in the samples presented here. In addition, none of the sulfides analysed in this study have $\delta^{34}S$ values of ~0 ‰, and therefore sulfur is not solely mantle derived (e.g., Alt and Shanks, 1998; Sakai et al., 1984; Shanks et al., 1995). Instead, the samples from Serra di Pigno and Capu Corvoli record a wide range of sulfur isotopic concentrations from 1.7–15.5 ‰. On the basis of textural observations and non-zero $\delta^{34}S$ values, it is concluded that primary sulfides are not preserved in the studied samples.

Serra di Pigno samples proximal to metasediments and metagabbros (CO13-33 and CO13-55) display different trends in changes to $\delta^{34}S$ values throughout the subduction cycle. The sample in close proximity to metagabbro and calcareous schist (CO13-55, section 4.2.3) shows a significantly different composition for the late sulfides (5.5–8.0‰) compared to earlier sulfides (1.9 to 6.5‰, Fig. 3c). However, there is no significant difference between prograde and retrograde sulfide grains in CO13-33 (Fig. 3b). The $\delta^{34}S$ values of sulfides in CO13-55 are also significantly lower than the sample distal to other lithologies ($p=1.81x10^{-5}$), with values of 1.9–8.0‰ and 4.3 to 10.4‰, respectively (Fig. 3a and c). Capu Corvoli chlorite schist and talc schist samples, that are proximal to metagabbro and only metres apart from each other, show very different $\delta^{34}S$ values; CO14-03 has heterogeneous sulfur isotope compositions ranging from 5.9 to 15.5‰, whereas CO14-04 has lower and more homogeneous $\delta^{34}S$ values of 3.6 to 5.4‰ (Fig. 3d and e).

The isotopic compositions of the sulfides are assessed in the context of trace element composition, bacterial sulfate reduction, hydrothermal sulfate reduction, sulfur speciation in

the fluid, rock buffering versus fluid buffering of the samples, the effects temperature during prograde metamorphism, and the effect of lithological mixing.

6.1. Trace element relationships with $\delta^{34}S$

Trace element mapping was carried out to determine the relationship between $\delta^{34}S$ and trace elements, which provide insights into fluid pathways and potential composition (e.g., Evans et al., 2014; Giacommetti et al., 2014). Whereas no significant correlation was observed between Co or Ni and $\delta^{34}S$ in CO14-03 (R^2 = 0.30 and 0.12, respectively) or Ni in CO14-04 (R^2=0.23), the correlation between Co and $\delta^{34}S$ in CO14-04 was found to be statistically significant at a 95% confidence level (P=0.048). Therefore, in general $\delta^{34}S$ is inferred to be decoupled from Ni and Co, with the exception of Co in CO14-04. The limited data available here, therefore, suggests that trace elements are not controlled by the same processes that determine the S isotope compositions in the pyrite grains. With the exception of Co in CO14-04, the lack of correlation between trace element zoning and $\delta^{34}S$ values is in agreement with previous studies on subducted sulfides (Giacommetti et al., 2014), although some correlation between Co and $\delta^{34}S$ was reported for pyrites in mafic and sedimentary rocks (Evans et al., 2014; Giacommetti et al., 2014). However, due to the restrictions of the beam size for analysis, it was not possible to assess the $\delta^{34}S$ zonation on the <5 μm scale of the Co and Ni zoning, so small length scale variations in S isotope compositions would have been obscured by the relatively large beam size (10 μm).

Similarly, it was not possible to determine relationships between trace element concentrations and sulfur isotope compositions in pentlandite grains due to the small size of the grains analysed, so areas selected for analysis were considered to be homogeneous in Co, Ni and As.

6.2. The effect of seafloor processes on sulfur geochemistry

The infiltration of sulfate-bearing seawater into mantle peridotite and consequent serpentinisation results in the addition of seawater-derived sulfur to the rock (Alt and Shanks, 1998; Delacour et al., 2008). In the case of Alpine Corsica, it is considered that primary mantle rocks were exposed on the seafloor and juxtaposed with the continental basement during Tethyan rifting in the Middle to Late Jurassic (Bathonian to Oxfordian) in an ultra-slow spreading centre or an ocean-continent transition setting (e.g., Vitale Brovarone et al., 2011; 2013). During this time, seawater sulfate had $\delta^{34}S$ values of ~ 17‰ (Kampschulte and Strauss, 2004). Hydrothermal alteration may also occur during initial subduction associated

with slab bending (Ranero and Sallares, 2004). The heterogeneity of $\delta^{34}S$ values in both the Serra di Pigno samples (with an overall range from 3.1 to 8.9‰) and the Capu Corvoli samples (3.6 to 15.5‰) implies that seawater sulfate was likely incorporated into the sulfides, and subsequent processes, including bacterial or hydrothermal sulfate reduction on the seafloor, and further fluid:rock interaction during subduction and exhumation, led to a loss of ^{34}S relative to ^{32}S

6.2.1 Bacterial sulfate reduction

Hydrogen and CH_4 released during seafloor serpentinisation, provides an energy source for sulfate reducing micro-organisms (e.g., Alt and Shanks, 1998; Schrenk et al., 2004; Kelley et al., 2005; Brazelton et al., 2006; Schwarzenbach et al., 2012, Schrenk et al., 2013 and references therein). Bacterial sulfate reduction (BSR) enriches the light isotope in the mineral products, therefore if BSR occurred during serpentinisation in an open system, negative $\delta^{34}S$ are expected (e.g., Schwarzenbach et al., 2012). Such a signal is not observed in the sulfides measured here. However, in a closed system, where there is limited fluid circulation, such as in deep sections of magma poor rifted margins (i.e., an ocean-continent transition zone, the proposed pre-subduction geodynamic setting of Alpine Corsica), BSR could enrich ^{34}S over precursor mantle values if the conversion of seawater sulfate to sulfide were close to completion. Nevertheless, if sulfides produced by microbial sulfate reduction were preserved, at least a few negative isotopic values would be expected as most sulfides would have grown in an open system, but this is not the case, therefore BSR is not thought to have played a significant role in the production of the sulfur isotope compositions of the samples described here.

6.2.2 Hydrothermal sulfate reduction

Recent studies have shown that $\Delta^{33}S$ in addition to $\delta^{34}S$ values can be used to distinguish between open or closed system sulfate reduction, and hydrothermal versus bacterial sulfate reduction (Ono et al., 2012; Schwarzenbach et al., 2018). $\Delta^{33}S$ values in the samples analysed here indicate a small but significant mass-independent fractionation (MIF) in three pentlandite grains from CO13-40, four pentlandite grains from CO13-55 and three pyrite grains in CO14-04. The data were carefully checked for any variations caused by a drop in S counts or beam centring, and the effects of crystallographic orientation on $\Delta^{33}S$ values is considered to be negligible (LaFlamme et al., 2016). Therefore, the $\Delta^{33}S$ values are concluded to result from MIF, whereby variation in isotope abundance is not dependent on

mass and thus records other processes. Insignificant $\Delta^{33}S$ values in most grains is probably a matter of precision. The maximum recorded $\Delta^{33}S$ values for peridotite from the Iberian Margin are 0.14–0.16‰ (Ono et al., 2012; Schwarzenbach et al. 2018), whereas in this study $\Delta^{33}S$ values in pentlandite grains are 0.33–0.67‰ and pyrite grains record $\Delta^{33}S$ values of between -0.17 and +0.11‰. Therefore, the pyrite and pentlandite measurements are less precise but within error of the measurements in Ono et al. (2012) and Schwarzenbach et al. (2018). Lower $\Delta^{33}S$ values in pyrite may be consistent with HSR in an open system, which typically produce more negative $\Delta^{33}S$ values. More precise measurements of $\Delta^{33}S$ are possible using bulk powders and mineral separates (Ono et al., 2012), but not with the *in-situ* SIMS technique used in this study, required for analysis of the small grains in the samples presented here.

With the exception of one grain (CO13-55 a2 s1-1), pentlandite grains with significant $\Delta^{33}S$ values are associated with prograde metamorphism and thus hydrothermal sulfate reduction occurred either during seafloor alteration or prograde metamorphism. In contrast, non-zero pyrite $\Delta^{33}S$ values are found in both early and late pyrite. It has been proposed that a MIF-derived signal could result from the breakdown or formation of S^{3-}, which could be present in fluids at depth in subduction zones in supercritical fluids (Pokrovski and Dubessy, 2015). Pokrovski and Dubessy (2015) proposed that the S^{3-} effect on MIF could result from its radical properties and resemblance to ozone (O_3). It is possible that the MIF signal reflects either HSR or mineral S^{3-} fractionation or a combination. For example, sulfate could have been hydrothermally reduced on the seafloor, and S^{3-} further could contribute to the MIF signal during subduction. At present, the lack of fractionation factors for the S^{3-} ion prevents a more detailed interpretation of the data.

6.3. The effects of temperature increase associated with prograde metamorphism

Temperature influences isotopic re-equilibration, fractionation factors and rates of diffusion during metamorphism (e.g., Bachinski, 1969; Ohmoto and Rye, 1979; Ohmoto and Lasaga, 1982). The effect of temperature on $\delta^{34}S$ depends on the speciation of sulfur. Sulfur is generally considered to be present as mineral-hosted S^-, S^{2-}, S^0 and sulfate (S^{6+}) in serpentinites (e.g., Alt et al., 2013; Debret et al., 2017; Merkulova et al., 2017). The effect of temperature on ^{34}S fractionation between fluid and sulfide minerals is greater for oxidised sulfur (SO_2 and SO_4^{2-}) than reduced sulfur (H_2S and HS^-). The speciation of aqueous sulfur in ultramafic rocks under prograde conditions is poorly constrained, though H_2S (e.g., Peretti

et al., 1992), SO_2 or SO_4^{2-} (e.g., Debret et al., 2016) are the most likely species. As discussed above, the S^{3-} ion has also been proposed to be present in high-pressure fluids such as those attributed to subduction zones (Pokrovski and Dubessy, 2015, Section 6.2.2).

The oxide and sulfide assemblages in the Serra di Pigno serpentinites and the prograde assemblage of CO14-04 from Capu Corvoli are low variance and are therefore inferred to be rock buffered with respect to sulfur, with low fluid:rock interaction and hence only local fluid flow. Activity-activity diagrams of oxide and sulfide stability as a function of aO_2 and aS_2 at high pressure (2 GPa, 555ºC) are presented in Evans et al. (2017). The prograde mineral assemblage in the serpentinites analysed (CO13-33, CO13-40 and CO13-55) is serpentine + pentlandite + magnetite ± pyrite, serpentine + pentlandite + magnetite ± heazlewoodite and in the hybrid sample, CO14-04, is talc + chlorite + magnetite + pyrite + pyrrhotite. According to calculated O_2 and S_2 activities associated with subduction (Evans et al., 2017), the oxide and sulfide assemblages present in the rock samples in this study are consistent with relatively low aO_2 and aS_2, therefore, reduced species such as H_2S or HS^- are inferred to be in solution.

Calculations were undertaken to assess the possible effect of isotope fractionation between sulfur hosted in the minerals and sulfur hosted in the fluids as an effect of prograde metamorphism. A minimum temperature of 250ºC was chosen to maximise the calculated effect of fractionation. Fractionation was calculated for isotope equilibrium between pyrrhotite of mantle sulfur isotope composition and fluid, pyrite with a nominal hydrothermal isotope composition and fluid, and recrystallized pentlandite and fluid ($\Delta_{\text{pyrrhotite-}H_2S}$, $\Delta_{\text{pyrite-}H_2S}$ and $\Delta_{\text{pentlandite-}H_2S}$, respectively) in closed and open (Rayleigh) systems. A starting composition of 0‰ was chosen for mantle pyrrhotite (Sakai et al., 1984; Shanks et al., 1995; Alt et al., 1998). Pyrrhotite was included in calculations because it is present in the hybrid samples (see section 3.2). 8‰ was chosen as the starting composition for hydrothermal pyrite, the average of pyrite isotopic analyses here. The value of 6.7‰ for the recrystallised pentlandite was taken from the average analyses of the pentlandite grains in the Serra di Pigno samples. There are currently no fluid-mineral isotope fractionation factors available for pentlandite, so it is assumed that fractionation factors would be similar to either violarite ($Fe^{2+}Ni_2S_4$; Li and Liu, 2006) or pyrrhotite (Ohmoto and Rye, 1979), or somewhere in between these two end members. Fractionation at 250 ºC is minor for both violarite (-1.2‰, Li and Liu, 2006) and pyrrhotite (0.1‰, Ohmoto and Rye, 1979). Therefore, $\Delta_{\text{pentlandite-}H_2S}$

would be minimal at temperatures of 250ºC and above, in both the closed and open system calculations (Fig. 10a, b). Likewise, $\Delta_{pyrite\text{-}H_2S}$ would also be minor at 250ºC, at 1.5‰ (Ohmoto and Rye, 1979). Therefore, fractionation between reduced sulfide species in solution and sulfide minerals would not be a first order control on the sulfur isotope compositions, hence sulfur isotope ratios reflect those in the fluid or sulfide minerals that have undergone seafloor alteration.

6.4. Retention of seafloor $\delta^{34}S$ in prograde sulfides

Sulfides texturally related to prograde to peak metamorphism include pentlandite in CO13-40, pn1 in CO13-33, in CO13-55 and py1 and po1 in CO14-04. $\delta^{34}S$ values in CO13-40 and CO13-33 are similar and range from 4.3 to 10.4‰ in CO13-40 and 6.5 to 8.8‰ in CO13-33. Pentlandite2 in CO13-55 has lower values (1.9 to 5.7‰). The positive $\delta^{34}S$ values suggest that sulfur isotope compositions were not significantly affected by seafloor BSR. In addition, the heterogeneous $\delta^{34}S$ values suggest that diffusion rates were too slow to affect sulfur isotope compositions. Peak metamorphic temperatures were ~414 to 470 ºC and high-pressure metamorphism is estimated to have occurred from ~55 to 34 Ma (Ravna et al., 2010, Vitale Brovarone et al., 2011, 2013). At such temperatures and time scale, diffusion of sulfur is predicted to be on the scale of >100 µm (Watson et al., 2009), inconsistent with the observed heterogeneous $\delta^{34}S$ values in the studied sulfides except pyrites in the talc schist sample, CO14-04, which have homogeneous S isotope compositions. However, sharp gradients in Co and Ni concentrations recorded in pyrite grains (Fig. 8b–f), and the metasomatic nature of this sample, suggest that fluid flow and mass transport and re-equilibration via dissolution-precipitation reactions are likely to prevail and solid state diffusion is inferred to be limited (e.g. Putnis, 2002; Putnis and Austrheim 2009). Therefore, the process of HSR during seafloor alteration is the preferred control on sulfur isotope ratios in prograde sulfides.

The preservation of sulfur isotope compositions derived from seafloor sulfate reduction is consistent with the conclusions of Alt et al. (2012a) who compared high-pressure serpentinites from the Voltri Massif and seafloor serpentinite considered unaffected by metamorphism from Val Graveglia, and found no difference in content or isotopic composition of sulfur during subduction on a sample scale. Bulk $\delta^{34}S$ values recorded by high-pressure serpentinites from 6.0 to 14.3‰ were suggested to reflect the retention of

sulfur from seafloor serpentinisation, where seafloor sulfur isotope compositions range from –4 to 9.8‰.

6.5. Sulfides associated with exhumation

The similar range of heterogeneous $\delta^{34}S$ values of prograde sulfides and sulfides associated with the onset of exhumation in serpentinites CO13-33 and CO13-55 is consistent with the interpretation of early HSR as the dominant control on sulfur isotope compositions, and the formation of exhumation-related sulfides from this sulfur reservoir. However, the homogeneity of $\delta^{34}S$ values in talc schist sample CO14-04, and higher $\delta^{34}S$ values of up to 8.0‰ and 15.5‰ in sulfides associated with advanced stages of exhumation in the serpentinite sample CO13-55 and chlorite schist CO14-03, respectively, suggest that subduction related fluids may have influenced the sulfur isotope composition of these late sulfides.

Late sulfide and oxide mineral asssemblages associated with exhumation in the Capu Corvoli samples, CO14-03 and CO14-04 are high variance, and are therefore fluid buffered with respect to sulfur. The presence of the mineral assemblage magnetite + pyrite is attributed to increased aS_2 and aO_2 (Evans et al., 2017), relative to the Serra di Pigno samples, reflecting more oxidising conditions in the hybrid environment. $\Delta_{pyrite\text{-}SO_2}$ and $\Delta_{pyrite\text{-}SO_4^{2-}}$ fractionation was calculated for the open and closed system models (Fig. 10c–f) using fractionation values from Ohmoto and Rye (1979). It is evident that there is greater fractionation between pyrite and SO_4, at ~23‰ (Fig. 10e, f), compared to pyrite and H_2S. Given the relatively texturally late setting of pyrite grains in the hybrid samples (section 3.2), with the exception of the early assemblage in CO14-04 (see 6.1.1), it is inferred that the hybrid samples record fluid buffering during exhumation and that during this time fluid:rock isotope fractionation could have been significant at a minimum temperature of 250 ºC, the temperature at which fractionation was calculated.

6.5.1. The source of heterogeneous $\delta^{34}S$ values in the chlorite schist.

The sulfur isotope composition of pyrites in CO14-03, with $\delta^{34}S$ values of up to 15.5‰, are higher than serpentinite $\delta^{34}S$ values, and are consistent with those of pyrites in Zermatt-Saas mafic eclogite samples associated with retrogression to blueschist facies (10.0–16.5‰, Evans et al., 2014, Fig. 11). The heterogeneity of the pyrites in CO14-03 likely reflects the mixing of fluids from different sources, as expected for a hybridised ultramafic/mafic rock.

Metasomatism and hybridisation of the rock either during seafloor alteration and/or prograde metamorphism, could have contributed sulfur with high $\delta^{34}S$ values to the rock (e.g. Alt and Shanks, 2003). Fluid mixing is possibly facilitated during deformation via fluid migration to low pressure zones (e.g., Evans et al., 2014). The similarity of some pyrite sulfur isotope compositions to those of retrogressed pyrites from mafic samples from the Zermatt-Saas provides additional evidence that metasomatic alteration and mixing with the metagabbro contributed oxidised sulfur-bearing fluids.

Fluid transport of sulfur on a sample scale or greater in CO14-03 is consistent with the observed high variance mineral assemblage, where the only late opaque minerals observed are large magnetite grains and pyrite, which replace prograde matrix minerals such as chlorite. The shift from magnetite to pyrite growth during late retrogression associated with exhumation records an increase in sulfur activity during this stage. The increase in sulfur activity probably occurred on relatively short time scales, given the aggregate nature of the pyrites in CO14-03, where such a texture suggests rapid growth and inadequate time to form well-defined crystal faces. Large clusters of aggregate pyrites record the highest $\delta^{34}S$ values, some of which surround magnetite grains (Fig. 2j). Rapid pyrite growth is likely consistent with a sudden influx of a sulfur-rich and, given the high $\delta^{34}S$ values, oxidised fluid at the onset of exhumation. We speculate that sulfate in solution was reduced to H_2S via interaction of sulfate bearing fluids with a pre-existing Fe^{2+}-bearing silicate, whereby Fe^{2+} was the electron donor for sulfate reduction. Fe^{2+}-bearing chlorite, a phase attributed to stability prior to fluid infiltration at the onset of exhumation, is a plausible candidate. The resultant oxidation from Fe^{2+} to Fe^{3+} within chlorite is consistent with the growth of magnetite at this stage. The reaction of H_2S with Fe^{3+} from magnetite, where ferric iron is considered to react faster than ferrous iron with H_2S (Canfield et al., 1992; Ono et al., 2012), may have triggered the rapid growth of pyrite, hence the observed clusters around magnetite.

6.5.2. The source of homogeneous $\delta^{34}S$ values in the talc schist.

CO14-04 pyrites record relatively low (4–5‰) and homogeneous $\delta^{34}S$ values. The transition from prograde metamorphism to exhumation is associated with a small but significant shift to lower $\delta^{34}S$ values in the pyrites. The shift from low to high variance sulfide mineral assemblages associated with this transition records a switch from a rock buffered or closed system to fluid buffered or open system with respect to sulfur. The low variance assemblage associated with prograde metamorphism is consistent with rock

buffering with H_2S or HS^- in solution. Therefore, in the talc schist sample, it is possible that the infiltration of external fluids homogenised pre-existing heterogeneous $\delta^{34}S$ values that were associated with pre-exhumation stages of metamorphism.

6.6. Implications for sulfur cycling

The *in-situ* $\delta^{34}S$ data presented here is consistent with the range of whole rock $\delta^{34}S$ values presented in Alt et al. (2012a) from the Voltri Massif in the Ligurian Alps, where the pre-subduction setting is similar to that of the samples studied here (Fig. 11). Alt et al. (2012) proposed that the sulfur isotope compositions of serpentinites remained unaltered during subduction. The *in-situ* technique, however, allows the evolution of $\delta^{34}S$ values to be assessed as a function of the stage of sulfide growth, and provides an insight into fluid:rock interaction. The observation that all sulfides record $\delta^{34}S$ values in between those of the mantle and Jurassic seawater-derived sulfate, suggests that sulfides record mixing between these two end members (Fig. 11). The textural preservation of sulfides with inclusions of antigorite, a high-pressure serpentine polymorph, and the overprinting of late antigorite generations by retrograde sulfides suggest sulfur redistribution on a millimetre scale during subduction. Spatially heterogeneous sulfur isotope compositions, similar chemical compositions of sulfides between early and late sulfides (section 5.1), and low variance mineral assemblages, is consistent with a closed system, and only local scale redistribution of sulfur with low fluid:rock ratios.

Sulfides associated with advanced stages of exhumation in serpentinite proximal to metagabbro and calcareous schist (CO13-55), record a significant shift towards higher $\delta^{34}S$ values, and record the presence of fluids with the ability to carry oxidised sulfur (SO_2 or SO_4^{2-}) at depth within subduction zones. Fluids bearing oxidised sulfur were most likely devolatilised from lithologies other than serpentinites during subduction, because the sulfide mineral assemblages in the Serra di Pigno serpentinites are consistent with reduced sulfur in solution.

The hybrid samples are fluid buffered on at least the scale of the pyrites (0.1 to 1cm) and the homogeneity of the early and late S isotope compositions of pyrite in CO14-04 suggests that fluids and therefore sulfur may have been sourced externally, consistent with the metasomatic alteration of this sample. The high variance mineral assemblage of CO14-03 is associated with heterogeneous $\delta^{34}S$ values, unlike the homogeneous values in CO14-04.

One possibility is that sulfur in this rock derived from both mafic and ultramafic sources, consistent with the hybrid nature of this sample.

The composition of fluids released during dehydration of serpentinites are poorly constrained, however a fluid inclusion study in high-pressure serpentinites from Cima di Gagnone, Swiss Alps, suggests the release of Cl-bearing fluids during the dehydration reactions of chrysotile, and antigorite + brucite (Scambelluri et al., 2004a; Scambelluri et al., 2004b; Kodolányi and Pettke, 2011; Scambelluri et al., 2015). On the basis of the presence of sulfides in the fluid inclusions, sulfur in such fluids is proposed to be hosted by a reduced species (Scambelluri et al., 2015). On the other hand, the low ferric iron contents and high Fe isotopic values of serpentinites have been suggested to record the devolatilisation of sulfate-bearing fluids during subduction (Debret et al., 2016), consistent with the presence of sulfate in seafloor serpentine minerals (Debret et al., 2017). In this study, on the basis of mineral assemblages in the Serra di Pigno serpentinites, the reduced species H_2S or HS^- are inferred to be in solution during subduction.

7. Conclusions

In-situ sulfur isotope data, in combination with textural and trace element compositions provides insights into the processes, evolution of the redox state and source of sulfur in serpentinites and hybrid mafic/ultramafic rocks through the subduction cycle. High $\delta^{34}S$ values were recorded in all sulfides (1.9–15.5‰), where the simplest explanation for this observation is the early fixation and retention of oxidised sulfur from seafloor alteration in the serpentinites. This explanation is consistent with heterogeneous values, low variance mineral assemblage and low degrees of fluid:rock interaction in most serpentinite samples, with the exception of a serpentinite sample proximal to metagabbro and calcareous schist, where there is a marked shift towards higher $\delta^{34}S$ values in pentlandite grains associated with late exhumation. Therefore, in the studied serpentinites, sulfur is redistributed only on a local mm to cm scale throughout the subduction cycle, consistent with the conclusions of previous sulfur isotope studies (e.g., Alt et al., 2012a). Infiltration of slab derived fluids during exhumation affected the sulfur mineral assemblages and sulfur isotope compositions in hybrid samples. Hybridisation of mafic/ultramafic rocks appears to be dominated by fluid-buffered assemblages with high sulfur activities, suggesting mobilisation of oxidised sulfur during ‘mixing’ of these lithologies on a scale greater than a thin-section sized sample.

Acknowledgements

Luke Daly and Sarah Hayes are thanked for the Capu Corvoli samples and for discussions on field observations of these samples. Malcolm Roberts is thanked for his assistance with the JEOL 8530 WDS microprobe at the Centre for Microscopy, Characterisation and Analysis (CMCA), the University of Western Australia (UWA). An anonymous reviewer and Alicia Cruz-Uribe are thanked for constructive reviews that helped to improve the quality of this manuscript. This work was supported by an Australian Research Council (ARC) Future Fellowship (FF12000579) to K.E. and a Curtin International Postgraduate Research Scholarship (CIPRS) to R.J.C. The authors would like to acknowledge the Australian Microscopy & Microanalysis Research Facility, AuScope, the Science and Industry Endowment Fund, and the State Government of Western Australian for contributing to the Ion Probe Facility at the Centre for Microscopy, Characterisation and Analysis at the University of Western Australia.

References

Agard, P., & Vitale-Brovarone, A. (2013). Thermal regime of continental subduction: the record from exhumed HP–LT terranes (New Caledonia, Oman, Corsica). *Tectonophysics*, **601**, 206-215.

Alt, J. C., Garrido, C. J., Shanks, W., Turchyn, A., Padrón-Navarta, J. A., Sánchez-Vizcaino, V. L., Pugnaire, M. T. G. & Marchesi, C. (2012b), 'Recycling of water, carbon, and sulfur during subduction of serpentinites: A stable isotope study of Cerro del Almirez, Spain', *Earth and Planetary Science Letters* **327**, 50–60.

Alt, J. C., Shanks, W. C., Bach, W., Paulick, H., Garrido, C. J., & Beaudoin, G. (2007). Hydrothermal alteration and microbial sulfate reduction in peridotite and gabbro exposed by detachment faulting at the Mid- Atlantic Ridge, 15° 20′ N (ODP Leg 209): A sulfur and oxygen isotope study. *Geochemistry, Geophysics, Geosystems*, **8**(8).

Alt, J. C., Shanks, W., Crispini, L., Gaggero, L., Schwarzenbach, E. M., Früh-Green, G. L. & Bernasconi, S. M. (2012a), 'Uptake of carbon and sulfur during seafloor serpentinization and the effects of subduction metamorphism in Ligurian peridotites', *Chemical Geology* **322**, 268–277.

Alt, J. C., Schwarzenbach, E. M., Früh-Green, G. L., Shanks III, W. C., Bernasconi, S. M., Garrido, C. J., ... & Marchesi, C. (2013). The role of serpentinites in cycling of carbon and sulfur: seafloor serpentinization and subduction metamorphism. *Lithos*, *178*, 40-54.

Alt, J. C. & Shanks, W. C. (2003), 'Serpentinization of abyssal peridotites from the MARK area, Mid-Atlantic Ridge: sulfur geochemistry and reaction modeling', *Geochimica et Cosmochimica Acta* **67**(4), 641–653.

Alt, J. C. & Shanks, W. C. (1998), 'Sulfur in serpentinized oceanic peridotites: Serpentinization processes and microbial sulfate reduction', *Journal of Geophysical Research: Solid Earth* **103**(B5), 9917–9929.

Alt, J. C., Shanks, W. C. & Jackson, M. C. (1993), 'Cycling of sulfur in subduction zones: The geochemistry of sulfur in the Mariana Island Arc and back-arc trough', *Earth and Planetary Science Letters* **119**(4), 477–494.

Aulbach, S., Stachel, T., Seitz, H.-M. & Brey, G. P. (2012), 'Chalcophile and siderophile elements in sulfide inclusions in eclogitic diamonds and metal cycling in a Paleoproterozoic subduction zone', *Geochimica et Cosmochimica Acta* **93**, 278–299.

Ault, W. & Jensen, M. (1963), 'Summary of sulfur isotope standards.', *In: Biogeochemistry of Sulfur Isotopes.Jensen ML (ed) Nat Sci Found, Symp Proc, Yale University*.

Bach, W., Garrido, C. J., Paulick, H., Harvey, J., & Rosner, M. (2004). Seawater- peridotite interactions: First insights from ODP Leg 209, MAR 15 N. *Geochemistry, Geophysics, Geosystems*, *5*(9).

Bachinski, D. J. (1969). Bond strength and sulfur isotopic fractionation in coexisting sulfides. *Economic Geology*, *64*(1), 56-65.

Barnes, S. J. (2000), 'Chromite in komatiites, II. Modification during greenschist to mid-amphibolite facies metamorphism', *Journal of Petrology* **41**(3), 387–409.

Barnes, S. J. & Roeder, P. L. (2001), 'The range of spinel compositions in terrestrial mafic and ultramafic rocks', *Journal of Petrology* **42**(12), 2279–2302.

Barnes, S. J., Heggie, G. J. & Fiorentini, M. L. (2013), 'Spatial variation in platinum group element concentrations in ore-bearing komatiite at the Long-Victor deposit, Kambalda Dome, Western Australia: enlarging the footprint of nickel sulfide orebodies', *Economic Geology* **108**(5), 913–933.

Bearden, J.A. (1964) "X-ray Wavelengths", Report NYO 10586, U.S. Atomic Energy Commission, Oak Ridge, Tennessee.

Bliss, N. & MacLean, W. (1975), 'The paragenesis of zoned chromite from central Manitoba',

Geochimica et Cosmochimica Acta **39**(6), 973–990.

Brazelton, W. J., Schrenk, M. O., Kelley, D. S. & Baross, J. A. (2006), 'Methane-and sulfur-metabolizing microbial communities dominate the Lost City hydrothermal field ecosystem', *Applied and Environmental Microbiology* **72**(9), 6257–6270.

Canfield D. E., Raiswell R. and Bottrell S. (1992) The reactivity of sedimentary iron minerals toward sulfide. Am. J. Sci. 292, 659-659.

Colás, V.; González-Jiménez, J. M.; Griffin, W. L.; Fanlo, I.; Gervilla, F.; O'Reilly, S. Y.; Pearson, N. J.; Kerestedjian, T. & Proenza, J. A. (2014), 'Fingerprints of metamorphism in chromite: New insights from minor and trace elements', *Chemical Geology* **389**, 137–152.

Crossley, R. J., Evans, K. A., Reddy, S. M., & Lester, G. W. (2017). Redistribution of Iron and Titanium in High- Pressure Ultramafic Rocks. *Geochemistry, Geophysics, Geosystems*, *18*(11), 3869-3890.

Debret, B., Andreani, M., Mucoz, M., Bolfan-Casanova, N., Carlut, J., Nicollet, C., Schwartz, S. & Trcera, N. (2014), 'Evolution of Fe redox state in serpentine during subduction', *Earth and Planetary Science Letters* **400**, 206–218.

Debret, B., Millet, M.-A., Pons, M.-L., Bouilhol, P., Inglis, E. & Williams, H. (2016), 'Isotopic evidence for iron mobility during subduction', *Geology* **44**(3), 215–218.

Debret, B., & Sverjensky, D. A. (2017). Highly oxidising fluids generated during serpentinite breakdown in subduction zones. *Scientific reports*, *7*(1), 10351.

Delacour, A., Früh-Green, G. L., Bernasconi, S. M. & Kelley, D. S. (2008), 'Sulfur in peridotites and gabbros at Lost City (30 N, MAR): Implications for hydrothermal alteration and microbial activity during serpentinization', *Geochimica et Cosmochimica Acta* **72**(20), 5090–5110.

Donovan, J. J., Kremser, D., & Fournelle, J. H. (2012). Probe for EPMA: acquisition, automation and analysis. *Probe Software, Inc., Eugene, Oregon*.

Duncumb, P. and Reed, S.J.B. (1968) *In:* Quantitative Electron Probe Microanalysis (K.F.J. Heinrich, ed.), Nat. Bureau Stand. Spl. Publ. **298**, 133.

Duncumb, P. and Shields, P.K. (1966) *In*: The Electron Microprobe (T.D. McKinley, K.F.J. Heinrich and D.B. Wittry, eds.), Wiley: New York, p. 284.

Ernst, W.G. & Liu, J., 1998. Experimental phase-equilibrium study of Al- and Ti-contents of calcic amphibole in MORB – a semiquantitative thermobarometer. *American Mineralogist*, **83**, 952–969.

Evans, B. W. & Frost, B. R. (1975), 'Chrome-spinel in progressive metamorphism—a preliminary analysis', *Geochimica et Cosmochimica Acta* **39**(6-7), 959–972.

Evans, B. W., & Kuehner, S. M. (2011). A nickel-iron analogue of balangeroite and gageite (Sasaguri, Kyushu, Japan). *European Journal of Mineralogy*, **23**(5), 717-720.

Evans, K. A. (2006). Redox decoupling and redox budgets: Conceptual tools for the study of earth systems. *Geology*, **34**(6), 489-492.

Evans, K. (2012), 'The redox budget of subduction zones', *Earth-Science Reviews* **113**(1), 11–32.

Evans, K. A., & Powell, R. (2015). The effect of subduction on the sulfur, carbon and redox budget of lithospheric mantle. *Journal of Metamorphic Geology*, **33**(6), 649-670.

Evans, K. A., Reddy, S. M., Tomkins, A. G., Crossley, R. J., & Frost, B. R. (2017). Effects of geodynamic setting on the redox state of fluids released by subducted mantle lithosphere. *Lithos*, **278**, 26-42.

Evans, K., Tomkins, A., Cliff, J. & Fiorentini, M. (2014), 'Insights into subduction zone sulfur recycling from isotopic analysis of eclogite-hosted sulfides', *Chemical Geology* **365**, 1–19.

Farquhar, J., Cliff, J., Zerkle, A. L., Kamyshny, A., Poulton, S. W., Claire, M., Adams, D. & Harms, B. (2013), 'Pathways for Neoarchean pyrite formation constrained by mass-independent sulfur isotopes', *Proceedings of the National Academy of Sciences* **110**(44), 17638–17643.

Faure, M. & Malavieille, J. (1981), 'Etude structurale d'un cisallement ductile: le charriage ophiolitique Corse dans la région de Bastia.', *Bulletin de la Societe Geologique de France, 23*.

Frost, B. R. (1991), 'Stability of oxide minerals in metamorphic rocks', *Reviews in Mineralogy and Geochemistry* **25**(1), 469–488.

Gervilla, F.; Padrón-Navarta, J.; Kerestedjian, T.; Sergeeva, I.; González-Jiménez, J. & Fanlo, I. (2012), 'Formation of ferrian chromite in podiform chromitites from the Golyamo

Kamenyane serpentinite, Eastern Rhodopes, SE Bulgaria: a two-stage process', *Contributions to Mineralogy and Petrology* **164**(4), 643–657.

Giacometti, F., Evans, K. A., Rebay, G., Cliff, J., Tomkins, A. G., Rossetti, P., Vaggelli, G. & Adams, D. T. (2014), 'Sulfur isotope evolution in sulfide ores from Western Alps: Assessing the influence of subduction-related metamorphism', *Geochemistry, Geophysics, Geosystems* **15**(10), 3808–3829.

Grieco, G. & Merlini, A. (2012), 'Chromite alteration processes within Vourinos ophiolite', *International Journal of Earth Sciences* **101**(6), 1523–1533.

Groppo, C., & Compagnoni, R. (2007). Metamorphic veins from the serpentinites of the Piemonte Zone, western Alps, Italy: a review. *Periodico di Mineralogia*, *76*, 127-153.

Harris, L., 1985. Progressive and polyphase deformation of the Schistes Lustrés in Cap Corse, Alpine Corsica. *Journal of Structural Geology* **7**, 637-650.

Heinrich, K.F.J. (1969) National Bureau of Standards, Technical Note 521.

Heinrich, K.F.J. (1986) *In:* Proc. 11th Intl. Conf. on X-ray Optics and Microanalysis (J.D. Brown and R.H. Packwood, eds.), Univ. Western Ontario, London, Ont. Canada, p. 67.

Ishihara, S. & Sasaki, A. (1989), 'Sulfur isotopic ratios of the magnetite-series and ilmenite-series granitoids of the Sierra Nevada batholith—a reconnaissance study', *Geology* **17**(9), 788–791.

Kampschulte, A. & Strauss, H. (2004), 'The sulfur isotopic evolution of Phanerozoic seawater based on the analysis of structurally substituted sulfate in carbonates', *Chemical Geology* **204**(3), 255–286.

Kelley, D. S., Karson, J. A., Früh-Green, G. L., Yoerger, D. R., Shank, T. M., Butterfield, D. A., Hayes, J. M., Schrenk, M. O., Olson, E. J., Proskurowski, G. & others (2005), 'A serpentinite-hosted ecosystem: the Lost City hydrothermal field', *Science* **307**(5714), 1428–1434.

Kimball, K. L. (1990), 'Effects of hydrothermal alteration on the compositions of chromian spinels', *Contributions to Mineralogy and Petrology* **105**(3), 337–346.

Kodolányi, J. & Pettke, T. (2011), 'Loss of trace elements from serpentinites during fluid-assisted transformation of chrysotile to antigorite—An example from Guatemala', *Chemical Geology* **284**(3), 351–362.

Labidi, J., Cartigny, P., Hamelin, C., Moreira, M., & Dosso, L. (2014). Sulfur isotope budget (32 S, 33 S, 34 S and 36 S) in Pacific–Antarctic ridge basalts: A record of mantle source heterogeneity and hydrothermal sulfide assimilation. *Geochimica et Cosmochimica Acta*, *133*, 47-67.

LaFlamme, C., Martin, L., Jeon, H., Reddy, Steven, M., Selvaraja, V., Caruso, S., Bui, Hao, T., Roberts, M. P., Voute, F., Hagemann, S., Wacey, D., Wing, B., Fiorentini, M. & Kilburn, M. R. (2016), 'In situ multiple sulfur isotope analysis by SIMS of pyrrhotite, pentlandite and chalcopyrite to refine magmatic ore genetic models', *Chemical Geology* **444**, 1–15.

Lahondère, D. & Guerrot, C. (1997), 'Datation Nd-Sm du métamorphisme éclogitique en Corse alpine: un argument pour l'existence, au Crétacé supérieur, d'une zone de subduction active localisée le long du block corse-sarde.', *Géologie de la France* **3**, 3-11.

Lahondère, J.; Lahondère, D.; Lluch, D.; Ohnenstetter, M.; Dominici, R. & Vautralle, C. (1992), 'Carte géologique de la France a 1/50000', *Luri, BRGM*.

Laird, J., & Albee, A. L. (1981). Pressure, temperature, and time indicators in mafic schist; their application to reconstructing the polymetamorphic history of Vermont. *American Journal of Science*, *281*(2), 127-175.

Li, X. P., Rahn, M., & Bucher, K. (2004). Serpentinites of the Zermatt- Saas ophiolite complex and their texture evolution. *Journal of Metamorphic Geology*, **22**(3), 159-177.

Li, Y. & Liu, J. (2006), 'Calculation of sulfur isotope fractionation in sulfides', *Geochimica et Cosmochimica Acta* **70**(7), 1789–1795.

Magott, R.; Fabbri, O. & Fournier, M. (2016), 'Subduction zone intermediate-depth seismicity: Insights from the structural analysis of Alpine high-pressure ophiolite-hosted pseudotachylyte (Corsica, France)', *Journal of Structural Geology* **87**, 95–114.

Marschall, H. R. & Shimizu, N. (2012), 'Sulfur Isotopes in High-Pressure Rocks', *Mineralogical Magazine* **76(6)**, 2070.

Marschall, H. R., & Schumacher, J. C. (2012). Arc magmas sourced from mélange diapirs in subduction zones. *Nature Geoscience*, **5**, 862–867.

Mattauer, M.; Faure, M. & Malavieille, J. (1981), 'Transverse lineation and large-scale structures related to Alpine obduction in Corsica', *Journal of Structural Geology* **3**(4), 401–409.

Mattauer, M.; Proust, F. & Etchecopar, A. (1977), 'Lineation "a" et mecanisme de cisaillement simple lie au chevauchement de la nappe des schistes lustres en Corse', *Bulletin de la Société Géologique de France* **7**(4), 841–847.

Mellini, M.; Rumori, C. & Viti, C. (2005), 'Hydrothermally reset magmatic spinels in retrograde serpentinites: formation of "ferritchromit" rims and chlorite aureoles', *Contributions to Mineralogy and Petrology* **149**(3), 266–275.

Meresse, F., Lagabrielle, Y., Malavieille, J., & Ildefonse, B. (2012). A fossil Ocean–Continent Transition of the Mesozoic Tethys preserved in the Schistes Lustrés nappe of northern Corsica. *Tectonophysics*, **579**, 4-16.

Merkulova, M. V., Muñoz, M., Brunet, F., Vidal, O., Hattori, K., Vantelon, D., ... & Huthwelker, T. (2017). Experimental insight into redox transfer by iron-and sulfur-bearing serpentinite dehydration in subduction zones. *Earth and Planetary Science Letters*, *479*, 133-143.

Merlini, A.; Grieco, G. & Diella, V. (2009), 'Ferritchromite and chromian-chlorite formation in mélange-hosted Kalkan chromitite (Southern Urals, Russia)', *American Mineralogist* **94**(10), 1459–1467.

Miller, J. A., & Cartwright, I. (2006). Albite vein formation during exhumation of high- pressure terranes: a case study from alpine Corsica. *Journal of Metamorphic Geology*, **24**(5), 409-428.

Mukherjee, R.; Mondal, S. K.; Rosing, M. T. & Frei, R. (2010), 'Compositional variations in the Mesoarchean chromites of the Nuggihalli schist belt, Western Dharwar Craton (India): potential parental melts and implications for tectonic setting', *Contributions to Mineralogy and Petrology* **160**(6), 865–885.

Mungall, J. E. (2002). Roasting the mantle: Slab melting and the genesis of major Au and Au-rich Cu deposits. *Geology*, *30*(10), 915-918.

Ohmoto, H. & Lasaga, A. C. (1982), 'Kinetics of reactions between aqueous sulfates and sulfides in hydrothermal systems', *Geochimica et Cosmochimica Acta* **46**(10), 1727–1745.

Ohmoto, H. & Rye, R. (1979), 'Isotopes of sulfur and carbon. Geochemistry of Hydrothermal Ore Deposits (Barnes, HL, ed.), 509-567', John Wiley & Sons Inc., New York.

Ono, S., Keller, N. S., Rouxel, O. & Alt, J. C. (2012), 'Sulfur-33 constraints on the origin of

secondary pyrite in altered oceanic basement', *Geochimica et Cosmochimica Acta* **87**, 323–340.

Padrón-Navarta, J. A., Sánchez-Vizcaíno, V. L., Hermann, J., Connolly, J. A., Garrido, C. J., Gómez-Pugnaire, M. T., & Marchesi, C. (2013). Tschermak's substitution in antigorite and consequences for phase relations and water liberation in high-grade serpentinites. *Lithos*, **178**, 186-196.

Paytan, A., Kastner, M., Campbell, D., & Thiemens, M. H. (1998). Sulfur isotopic composition of Cenozoic seawater sulfate. *Science*, **282**(5393), 1459-1462.

Paytan, A., Kastner, M., Campbell, D., & Thiemens, M. H. (2004). Seawater sulfur isotope fluctuations in the Cretaceous. *science*, *304*(5677), 1663-1665.

Peretti, A., Dubessy, J., Mullis, J., Frost, B. R. & Trommsdorff, V. (1992), 'Highly reducing conditions during Alpine metamorphism of the Malenco peridotite (Sondrio, northern Italy) indicated by mineral paragenesis and H2 in fluid inclusions', *Contributions to Mineralogy and Petrology* **112**(2-3), 329–340.

Peters, M., Strauss, H., Farquhar, J., Ockert, C., Eickmann, B., & Jost, C. L. (2010). Sulfur cycling at the Mid-Atlantic Ridge: A multiple sulfur isotope approach. *Chemical Geology*, *269*(3-4), 180-196.

Philibert, J. (1963) In Proc. 34th Intl. Symp. X-ray Optics and X-ray Microanalysis, Stanford University (H.H. Pattee, V.E. Cosslett and A. Engstrom, eds.) Academic Press: New York, p. 379.

Pokrovski, G. S. & Dubessy, J. (2015), 'Stability and abundance of the trisulfur radical ion in hydrothermal fluids', *Earth and Planetary Science Letters* **411**, 298–309.

Putnis A (2002) Mineral replacement reactions: from macroscopic observations to microscopic mechanisms, Mineralogical Magazine, **66**, 689–708.

Putnis, A., & Austrheim, H. (2010). Fluid- induced processes: metasomatism and metamorphism. *Geofluids*, **10**(1- 2), 254-269.

Ranero, C. & Sallares, V. (2004), 'Geophysical evidence for hydration of the crust and mantle of the Nazca plate during bending at the north Chile trench', *Geology* **32**(7), 549–552.

Ravna, E., Andersen, T. B., Jolivet, L. & De Capitani, C. (2010), 'Cold subduction and the

formation of lawsonite eclogite–constraints from prograde evolution of eclogitized pillow lava from Corsica', *Journal of Metamorphic Geology* **28**(4), 381–395.

Reed, S. J. B. (1965). Characteristic fluorescence corrections in electron-probe microanalysis. *British Journal of Applied Physics*, **16**(7), 913.

Rees, C., Jenkins, W. & Monster, J. (1978), 'The sulfur isotopic composition of ocean water sulfate', *Geochimica et Cosmochimica Acta* **42**(4), 377–381.

Richards, J. P. (2015). The oxidation state, and sulfur and Cu contents of arc magmas: implications for metallogeny. *Lithos*, **233**, 27-45.

Sakai, H., Des Marais, D., Ueda, A. & Moore, J. (1984), 'Concentrations and isotope ratios of carbon, nitrogen and sulfur in ocean-floor basalts', *Geochimica et Cosmochimica Acta* **48**(12), 2433–2441.

Santiago Ramos, D., Shimizu, N. & Scambelluri, M. (2012), Sulfur isotopic variations during subduction of hydrated lithosphere: the Erro Tobbio case, *in* 'AGU Fall Meeting Abstracts', pp. 04.

Scambelluri, M., Fiebig, J., Malaspina, N., Müntener, O. & Pettke, T. (2004b), 'Serpentinite subduction: implications for fluid processes and trace-element recycling', *International Geology Review* **46**(7), 595–613.

Scambelluri, M., Müntener, O., Ottolini, L., Pettke, T. T. & Vannucci, R. (2004a), 'The fate of B, Cl and Li in the subducted oceanic mantle and in the antigorite breakdown fluids', *Earth and Planetary Science Letters* **222**(1), 217–234.

Scambelluri, M.; Pettke, T.; Rampone, E.; Godard, M. & Reusser, E. (2014), 'Petrology and trace element budgets of high-pressure peridotites indicate subduction dehydration of serpentinized mantle (Cima di Gagnone, Central Alps, Switzerland)', *Journal of Petrology*, **55**(3), 459–498.

Scambelluri, M., Pettke, T. & Cannat, E. (2015), 'Fluid-related inclusions in Alpine high-pressure peridotite reveal trace element recycling during subduction-zone dehydration of serpentinized mantle (Cima di Gagnone, Swiss Alps)', *Earth and Planetary Science Letters* **429**, 45–59.

Schrenk, M., Kelley, D., Bolton, S. & Barossa, J. (2004) Low archaeal diversity linked to subseafloor geochemical processes at the Lost City Hydrothermal Flield, Mid-Atlantic Ridge. Environmental Microbiology, **6**, 1086–1095.

Schrenk, M. O., Brazelton, W. J., & Lang, S. Q. (2013). Serpentinization, carbon, and deep life. *Reviews in Mineralogy and Geochemistry*, **75**(1), 575-606.

Schwarzenbach, E. M., Früh-Green, G. L., Bernasconi, S. M., Alt, J. C., Shanks III, W. C., Gaggero, L., & Crispini, L. (2012). Sulfur geochemistry of peridotite-hosted hydrothermal systems: comparing the Ligurian ophiolites with oceanic serpentinites. *Geochimica et Cosmochimica Acta*, *91*, 283-305.

Schwarzenbach, E. M., Gill, B. C., & Johnston, D. T. (2018). Unraveling multiple phases of sulfur cycling during the alteration of ancient ultramafic oceanic lithosphere. *Geochimica et Cosmochimica Acta*, *223*, 279-299.

Seal, R. R. (2006), 'Sulfur isotope geochemistry of sulfide minerals', *Reviews in mineralogy and geochemistry* **61**(1), 633–677.

Seyler, M., Lorand, J. P., Dick, H. J., & Drouin, M. (2007). Pervasive melt percolation reactions in ultra-depleted refractory harzburgites at the Mid-Atlantic Ridge, 15 20′ N: ODP Hole 1274A. *Contributions to Mineralogy and Petrology*, **153**(3), 303.

Shanks, W., Bцhlke, J. & Seal, R. (1995), 'Stable Isotopes in Mid-Ocean Ridge Hydrothermal Systems: Interactions Between Fluids, Minerals, and Organisms', *Seafloor Hydrothermal Systems: Physical, Chemical, Biological, and Geological Interactions*, 194–221.

Shanks, W., Bischoff, J. L. & Rosenbauer, R. J. (1981), 'Seawater sulfate reduction and sulfur isotope fractionation in basaltic systems: interaction of seawater with fayalite and magnetite at 200–350 C', *Geochimica et Cosmochimica Acta* **45**(11), 1977–1995.

Shimizu N, Scambelluri M, S. R. D. &. T. S. (2013), 'Boron and Sulfur Isotopic Variations during Subduction of Hydrated Lithosphere: The Erro Tobbio Case', *Mineralogical Magazine* **77(5)**, 2201.

Spandler, C., Hermann, J., Faure, K., Mavrogenes, J. A. & Arculus, R. J. (2008), 'The importance of talc and chlorite "hybrid" rocks for volatile recycling through subduction zones, evidence from the high-pressure subduction mélange of New Caledonia', *Contributions to Mineralogy and Petrology* **155**(2), 181–198.

Spandler, C., & Pirard, C. (2013). Element recycling from subducting slabs to arc crust: A review. *Lithos*, **170**, 208-223.

Spear, F.S., 1981. An experimental study of hornblende stability and compositional variability in amphibolite. *American Journal of Science*, **281**, 697–734.

Tostevin, R., Turchyn, A. V., Farquhar, J., Johnston, D. T., Eldridge, D. L., Bishop, J. K. & McIlvin, M. (2014), 'Multiple sulfur isotope constraints on the modern sulfur cycle', *Earth and planetary science letters* **396**, 14–21.

Ueda, A. & Sakai, H. (1984), 'Sulfur isotope study of Quaternary volcanic rocks from the Japanese Islands Arc', *Geochimica et Cosmochimica Acta* **48**(9), 1837–1848.

Vitale Brovarone, A., Beltrando, M., Malavieille, J., Giuntoli, F., Tondella, E., Groppo, C., Beyssac, O. & Compagnoni, R. (2011), 'Inherited ocean–continent transition zones in deeply subducted terranes: insights from Alpine Corsica', *Lithos* **124**(3), 273–290.

Vitale Brovarone, A., Beyssac, O., Malavieille, J., Molli, G., Beltrando, M. & Compagnoni, R. (2013), 'Stacking and metamorphism of continuous segments of subducted lithosphere in a high-pressure wedge: the example of Alpine Corsica (France)', *Earth-Science Reviews* **116**, 35–56.

Vitale Brovarone, A. & Herwartz, D. (2013), 'Timing of HP metamorphism in the Schistes Lustrés of Alpine Corsica: New Lu–Hf garnet and lawsonite ages', *Lithos* **172**, 175–191.

Wacey, D., Kilburn, M. R., Saunders, M., Cliff, J. & Brasier, M. D. (2011), 'Microfossils of sulfur-metabolizing cells in 3.4-billion-year-old rocks of Western Australia', *Nature Geoscience* **4**(10), 698–702.

Wallace, P. J. & Edmonds, M. (2011), 'The sulfur budget in magmas: evidence from melt inclusions, submarine glasses, and volcanic gas emissions', *Reviews in Mineralogy and Geochemistry* **73**(1), 215–246.

Warburton, J., 1986. The ophiolite-bearing Schistes Lustrés nappe in Alpine Corsica: A model for the emplacement of ophiolites that have suffered HP/LP metamorphism. In: Blueschists and Eclogites (B.W. Evans and E.H. Brown, eds). *Geological Society of America Memoir*, **164**, 313-331.

Watson, E. B., Cherniak, D. J., & Frank, E. A. (2009). Retention of biosignatures and mass-independent fractionations in pyrite: Self-diffusion of sulfur. *Geochimica et Cosmochimica Acta*, **73**(16), 4792-4802.

Wylie, A. G.; Candela, P. A. & Burke, T. M. (1987), 'Compositional zoning in unusual Zn-rich chromite from the Sykesville District of Maryland and its bearing on the origin of" ferritchromit"', *American Mineralogist* **72**(3-4), 413–422.

Figure Captions

Figure 1: (a) map showing the locations and P-T conditions of the field areas Serra di Pigno and Capu Corvoli on Cap Corse, Corsica (redrawn from Brovarone et al., 2011, 2013). Abbreviations correspond to the name of the units; Mm: Monte Maggiore peridotite unit, Ce: Centuri continental slice, Ma: Macinaggio flysch, Fa: Farinole continental slice, Ne: Nebbio unit; Te: Tenda unit. **(b)** map of Serra di Pigno sample localities. **(c)** map of Capu Corvoli sample localities (adapted from Lahondère, 1992). MB = metabasalt, CS = calcareous schist, H = hybrid, MG = metagabbro. **(d)** Field photo showing the juxtaposition of lithologies at Serra di Pigno. **(e)** Field photo of the contact between metagabbro and chlorite schist at Capu Corvoli.

Figure 2: microphotographs illustrating key textures, bse = backscattered electron, rfl = reflected light and xpl = cross-polarised light image. **Serra di Pigno serpentinite samples:** (a) rfl: pentlandite grain in CO13-40 with early antigorite inclusions (atg1) replacement by atg2. (b) rfl: pentlandite (pn1) in CO13-33 aligned with atg1 foliation. (c) rfl: pn2 overprints early Cr- rich spinel grains in CO13-33. (d) rfl: pn3 grains in CO13-33 cross-cut late antigorite and associated with magnetite (mt2) (e) bse: pn1 cross-cut by atg3 in CO13-55 (f) xpl: pn2 associated with atg2 in CO13-55 (f) rfl: pn2 associated with atg2 in CO13-55 (h) xpl: euhedral grain of pn3 associated with late atg3 veins in CO13-55. **Capu Corvoli hybrid samples**: (i) rfl: pyrite grains within matrix in chlorite schist CO14-03. (j) pyrite rims on magnetite, and pyrite connected to the matrix by fractures in magnetite in chlorite schist CO14-03. (k) rfl: py1 grains in talc schist CO14-04 with inclusions of chromite and an iron hydroxide rim, which contains inclusions of po. (l) xpl: py2 grains with a talc2 rim in talc schist CO14-04 (xpl).

Figure 3: Histograms of $\delta^{34}S$ values in sulfides for (a) CO13-40, (b) CO13-33, (c) CO13-55, (d) CO14-03 and (e) CO14-04. Red/no lines= sulfide grains related to prograde and peak metamorphism. Blue/horizontal lines = sulfide grains related to early exhumation. Green/diagonal lines = sulfide grains related to late exhumation.

Figure 4: CO13-40. Reflected light images of pentlandite grains (a) s1 in area 3, (b) s8 in area 3, (c) s2 in area 1, (d) s9 + repeated analysis (r) in area 3 and (e) s3 in area 3. (f) NanoSIMS map of grain s3 in area 3, circle indicates point of SIMS analysis. All values are

$\delta^{34}S$ (‰) unless otherwise indicated. **Figure 1:** CO13-33. Reflected light images of pentlandite grains (a) Pn1 grain s14 in area 3, (b) Pn2 grain s4 in area 2, (c) Pn2 grain s3 in area 2, (d) Pn3 grain s10 in area 2 and (e) Pn3 grain s10 in area 3. (f) Co map (wt%) of a pn2 grain. All values are $\delta^{34}S$ (‰).

Figure 5: CO13-33. Reflected light images of pentlandite grains (a) Pn1 grain s14 in area 3, (b) Pn2 grain s4 in area 2, (c) Pn2 grain s3 in area 2, (d) Pn3 grain s10 in area 2 and (e) Pn3 grain s10 in area 3. (f) Co map (wt%) of a pn2 grain. All values are $\delta^{34}S$.

Figure 6: CO13-55 pentlandite. (a) bse image of Pn2 grain s2 in area 3. (b) Co map (wt%) of Pn2 grain s1in area 3. (c) bse image of Pn2 grain s1 in area 2. (d) bse image of Pn3 grain s2 in area 3. (e) bse image of Pn4 grain s3 in area 1. (f) bse image of Pn4 grain s1 in area 1. All values are $\delta^{34}S$ (‰).

Figure 7: CO14-03. Reflected light images of gold coated (a) matrix grain within 1mm of magnetite, area 1 analyses 1-8. (b) matrix grain area 2 analyses 9-13 (c) matrix grain area 3 within 1mm of magnetite analyses 9–11. (d) large cluster of pyrite aggregates in matrix area 2 1–8. (e) large cluster of pyrite grains on rim of large magnetite, area 3 analyses 1–11. All values are $\delta^{34}S$ (‰).

Figure 8: (a) reflected light image of matrix pyrite grain in CO14-03, area 1 analyses 1-8 for matrix pyrite, the same grain is shown in images b-c; (b) EPMA derived trace element map of Co in pyrite grain in CO14-03; (c) EPMA derived trace element map of Ni; (d) reflected light image of py2 grain s1 in area 1 in CO14-04; the same grain is shown in images e–f; (e) EPMA derived trace element map of Co in pyrite grain in CO14-04 (f) EPMA derived trace element map of Ni in pyrite grain in CO14-04; (g) Ni (wt%) plotted against $\delta^{34}S$ in CO14-03 and CO14-04; (h) Co (wt%) plotted against $\delta^{34}S$ in CO14-04. The values in b–c and e–f are $\delta^{34}S$ (‰). Sample CO14-03 = orange circles and sample CO14-04 = yellow diamonds in g–h.

Figure 9: CO14-04. Reflected light images of gold coated py1 grains (a) s2 in area 2, (b) s3 in area 2, (c) s1 in area 3, (d) s2 in area 3 and py2 grains in (e) s1 in area 1 and (f) s1 in area 2. All values are $\delta^{34}S$ (‰).

Figure 10: Fractionation calculation plots of $\delta^{34}S$ and progression of the reactions mantle (m) pyrrhotite-H_2S, mantle pentlandite-H_2S, hydrothermally altered and recrystallized (r) pyrrhotite-H_2S, hydrothermally altered and recystallised (r) pentlandite-H_2S, and hydrothermal pyrite-H_2S for (a) a closed system and (b) open system (Rayleigh) fractionation, between $\delta^{34}S$ and progression of the reactions mantle (m) pyrrhotite-SO_2,

mantle pentlandite-SO_2 and hydrothermal pyrite-SO_2 for (c) a closed system and (d) an open system (Rayleigh), and between $\delta^{34}S$ and progression of the reactions mantle (m) pyrrhotite-SO_4^{2-}, mantle pentlandite-SO_4^{2-} and hydrothermal pyrite-SO_4^{2-} for (c) a closed system and (d) an open system (Rayleigh), and between $\delta^{34}S$ and progression of the reactions mantle (m) pyrrhotite-SO_4^{2-}, mantle pentlandite-SO_4^{2-} and hydrothermal pyrite-SO_4^{2-} for (e) a closed system and (f) an open system (Rayleigh).

Figure 11: Comparison of $\delta^{34}S$ values from this study to those from other whole rock and *in-situ* studies.

Figure 1

Click here to download high resolution image

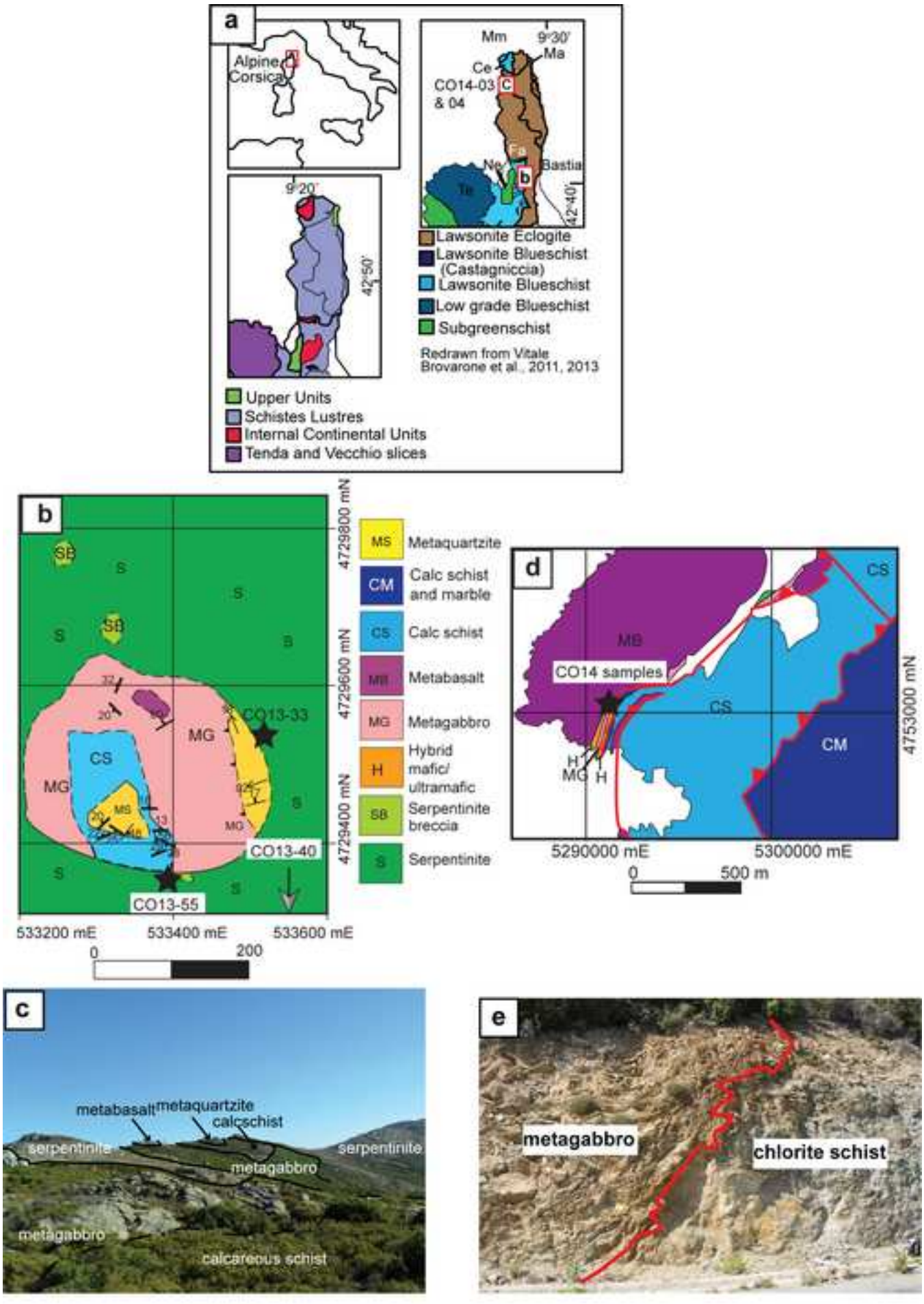

Figure 2

Click here to download high resolution image

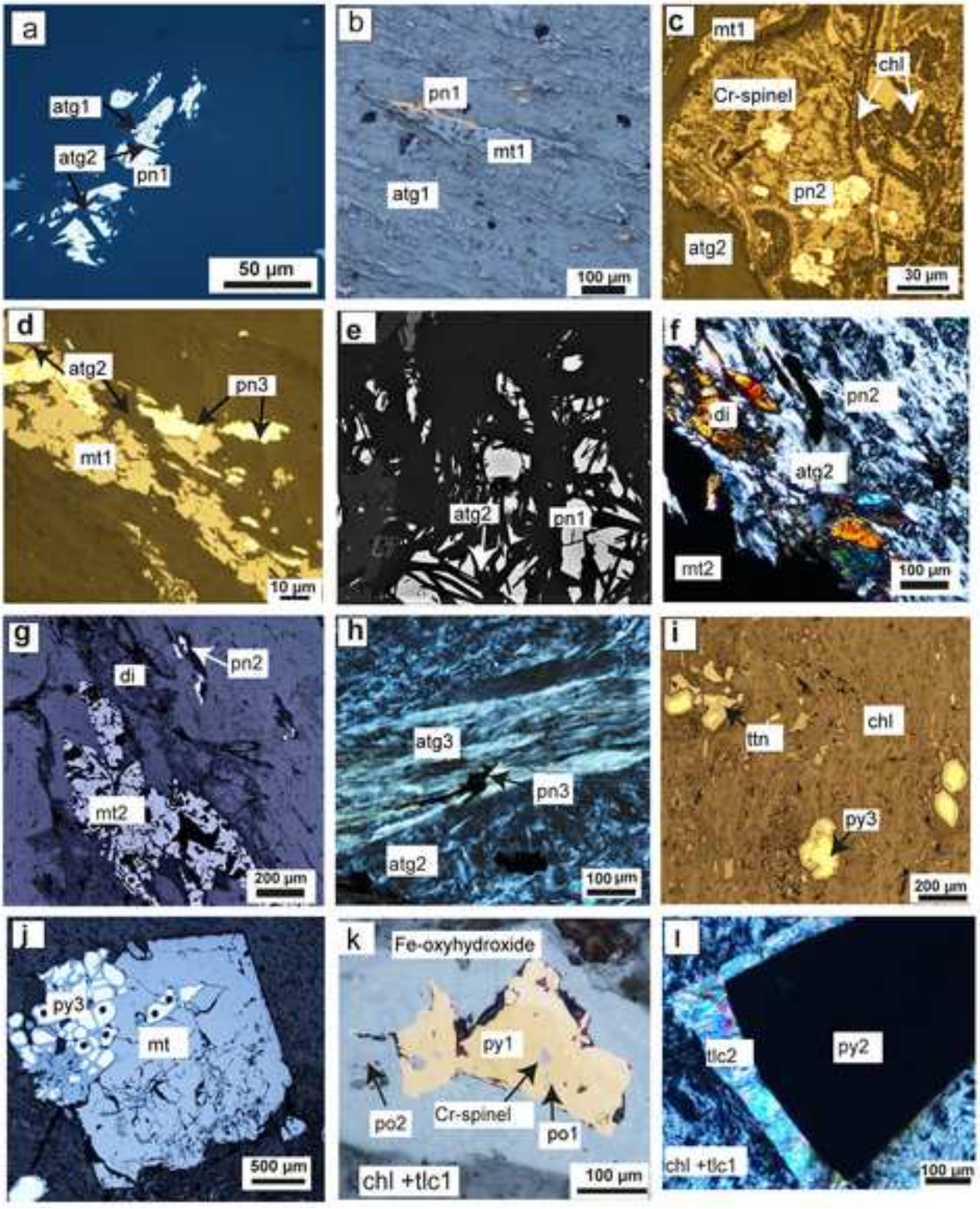

Figure 3

Click here to download high resolution image

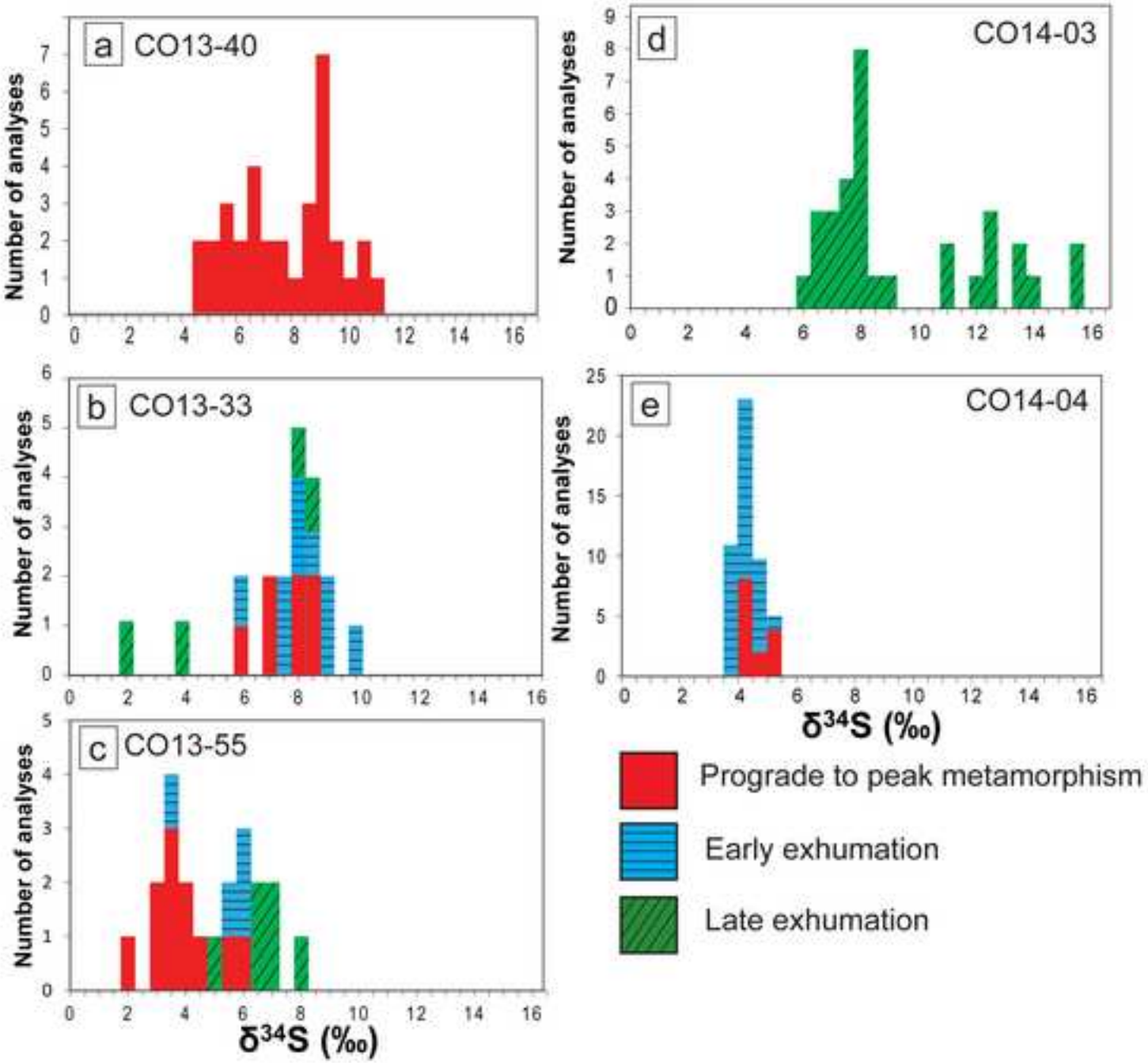

Figure 4

Click here to download high resolution image

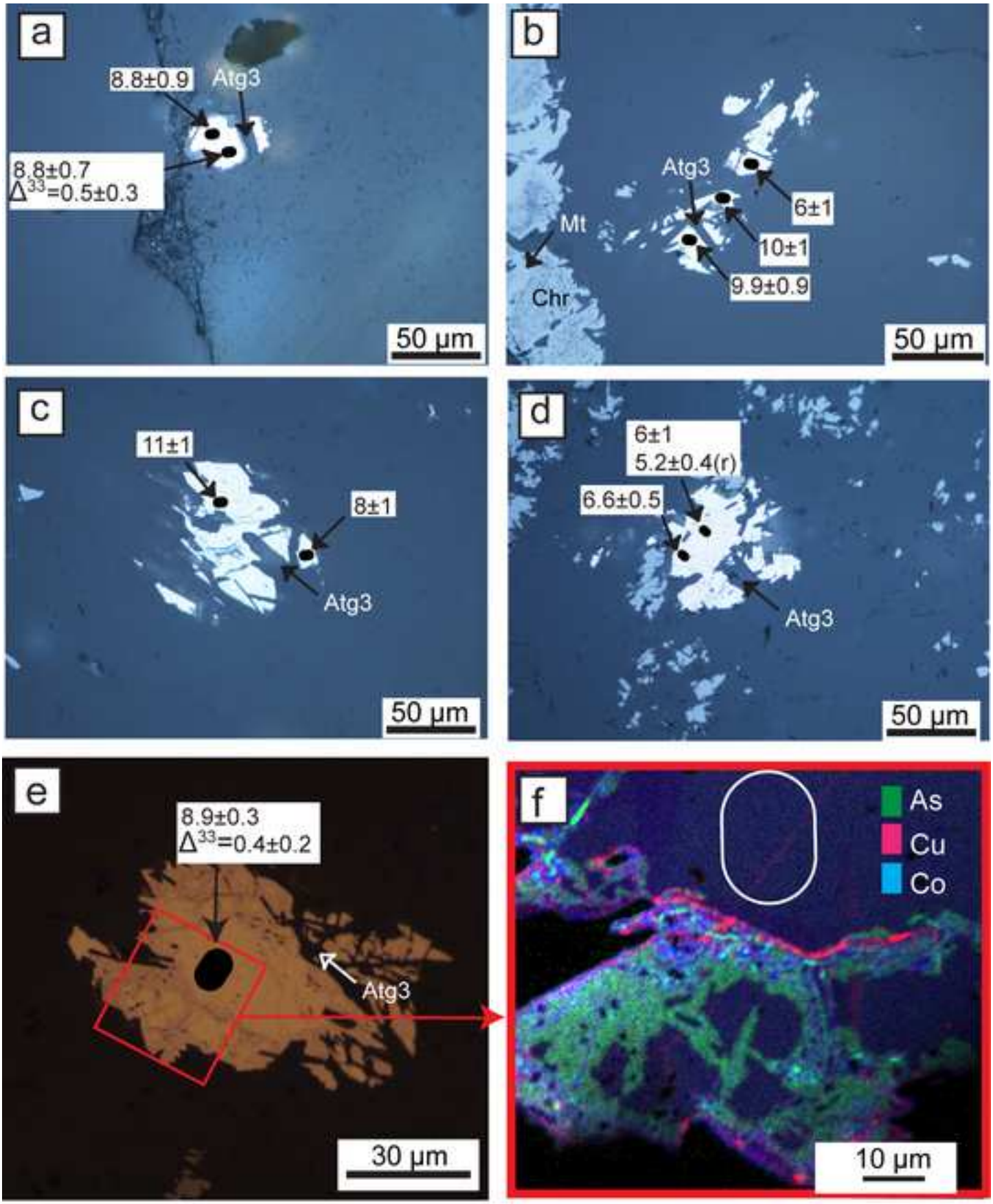

Figure 5

Click here to download high resolution image

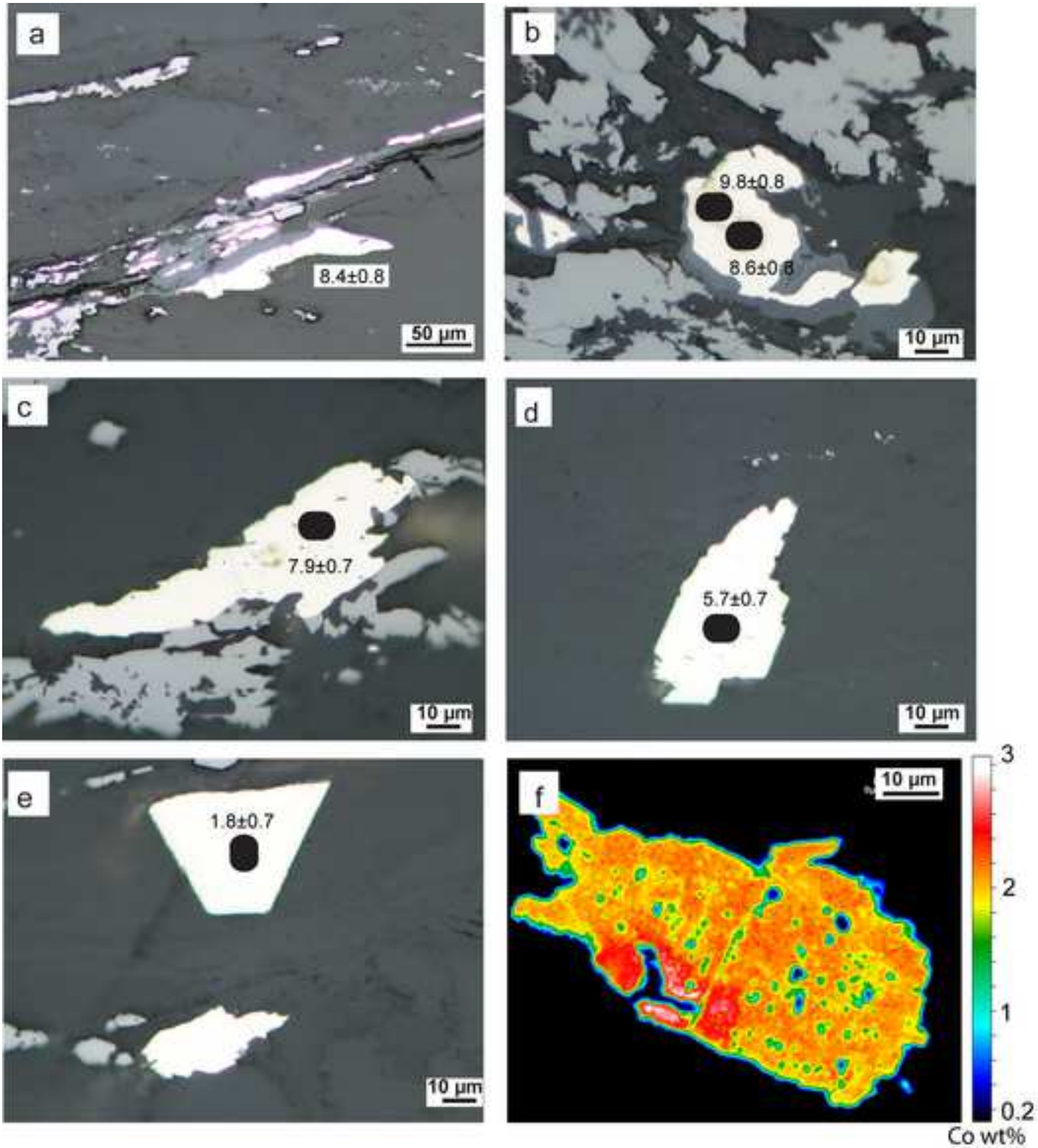

Figure 6

Click here to download high resolution image

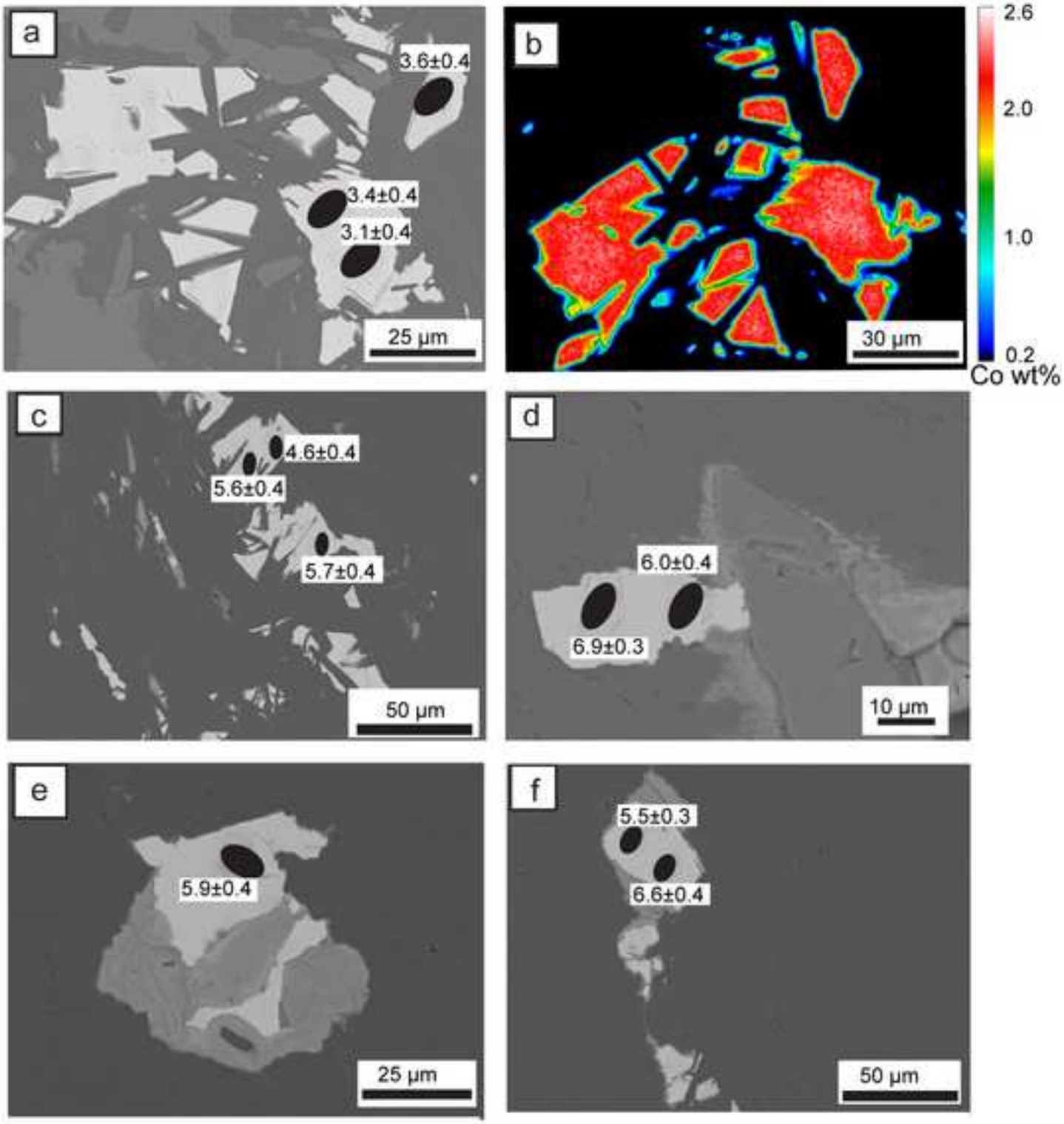

Figure 7

Click here to download high resolution image

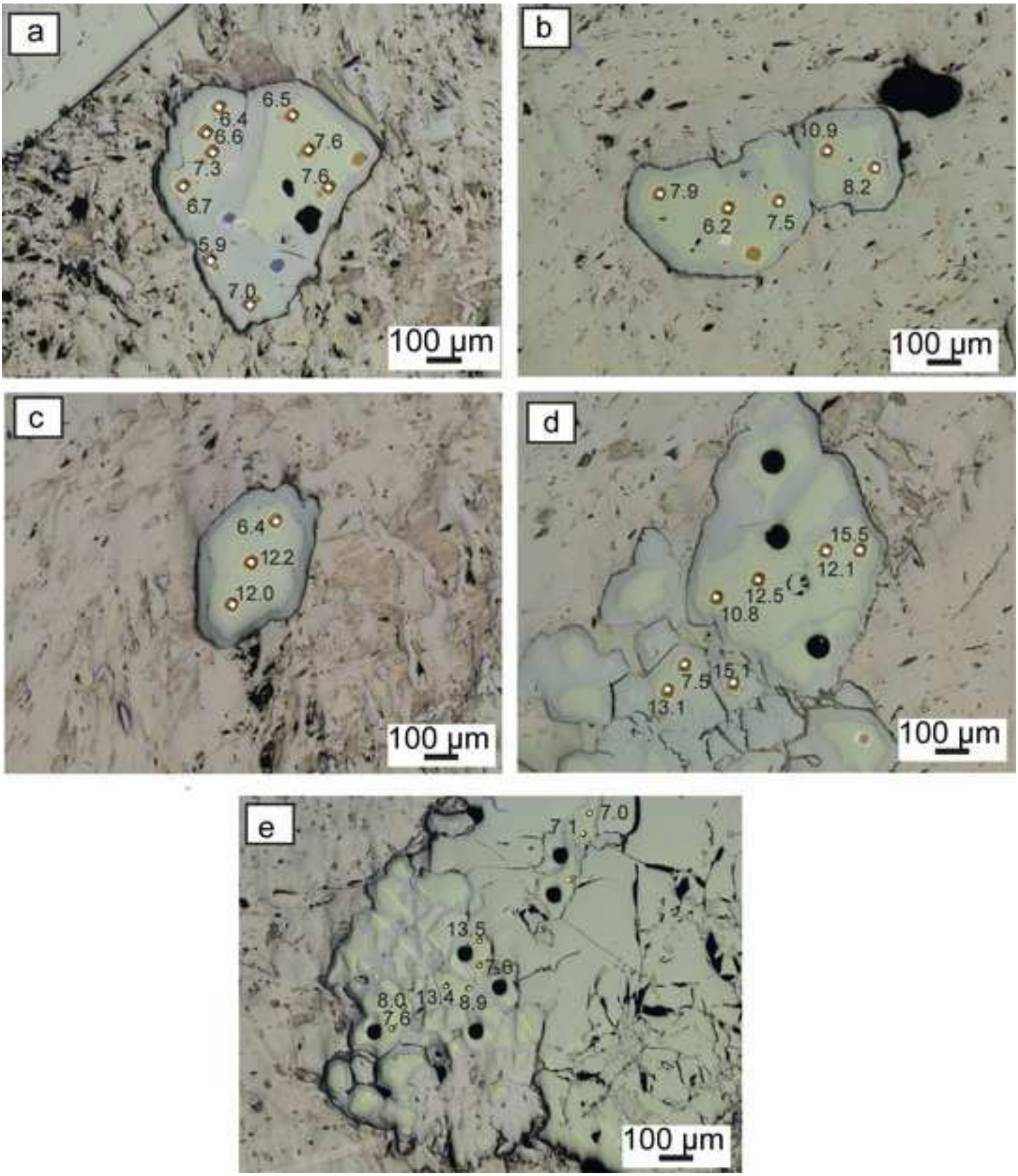

Figure 8

Click here to download high resolution image

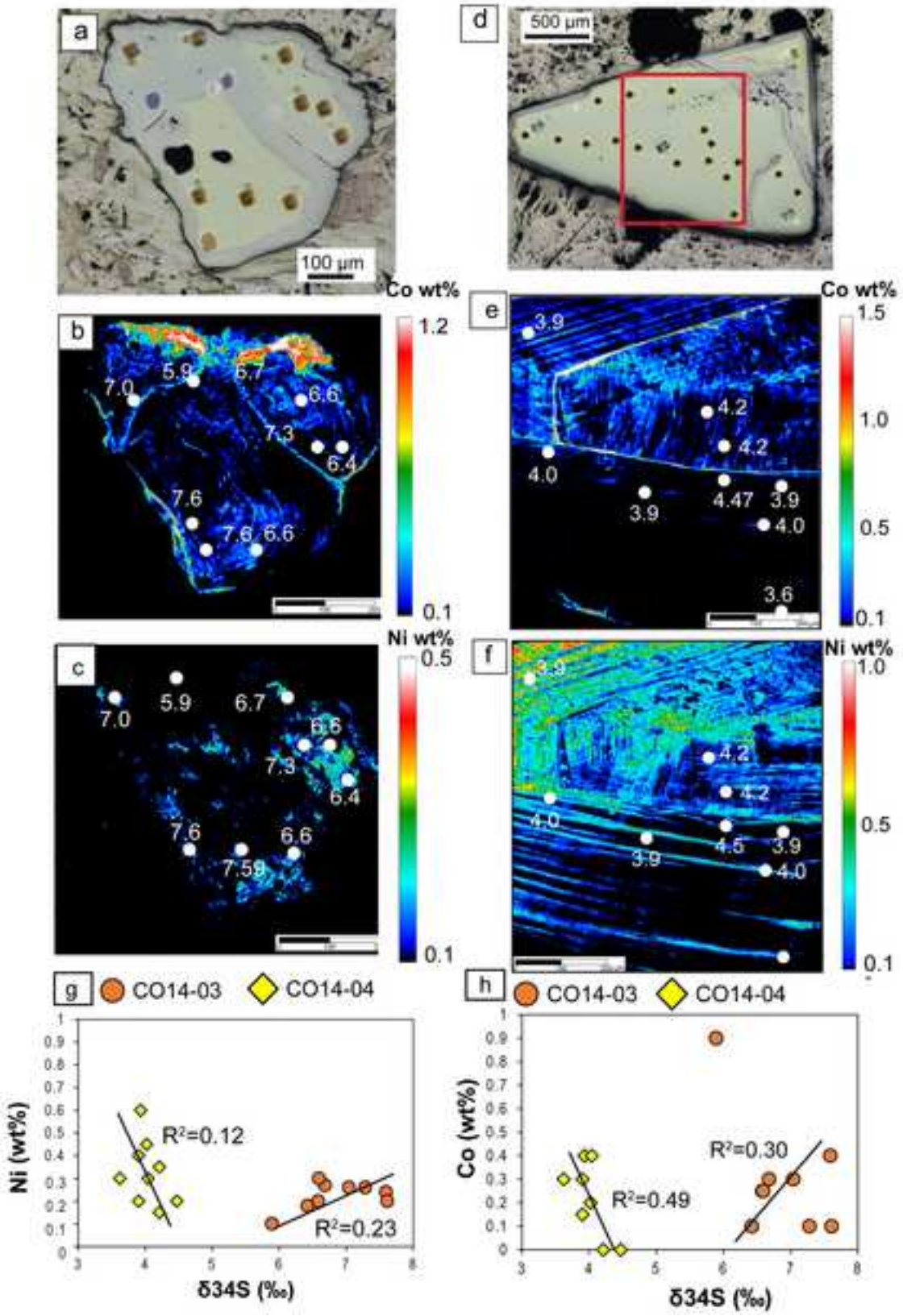

Figure 9

Click here to download high resolution image

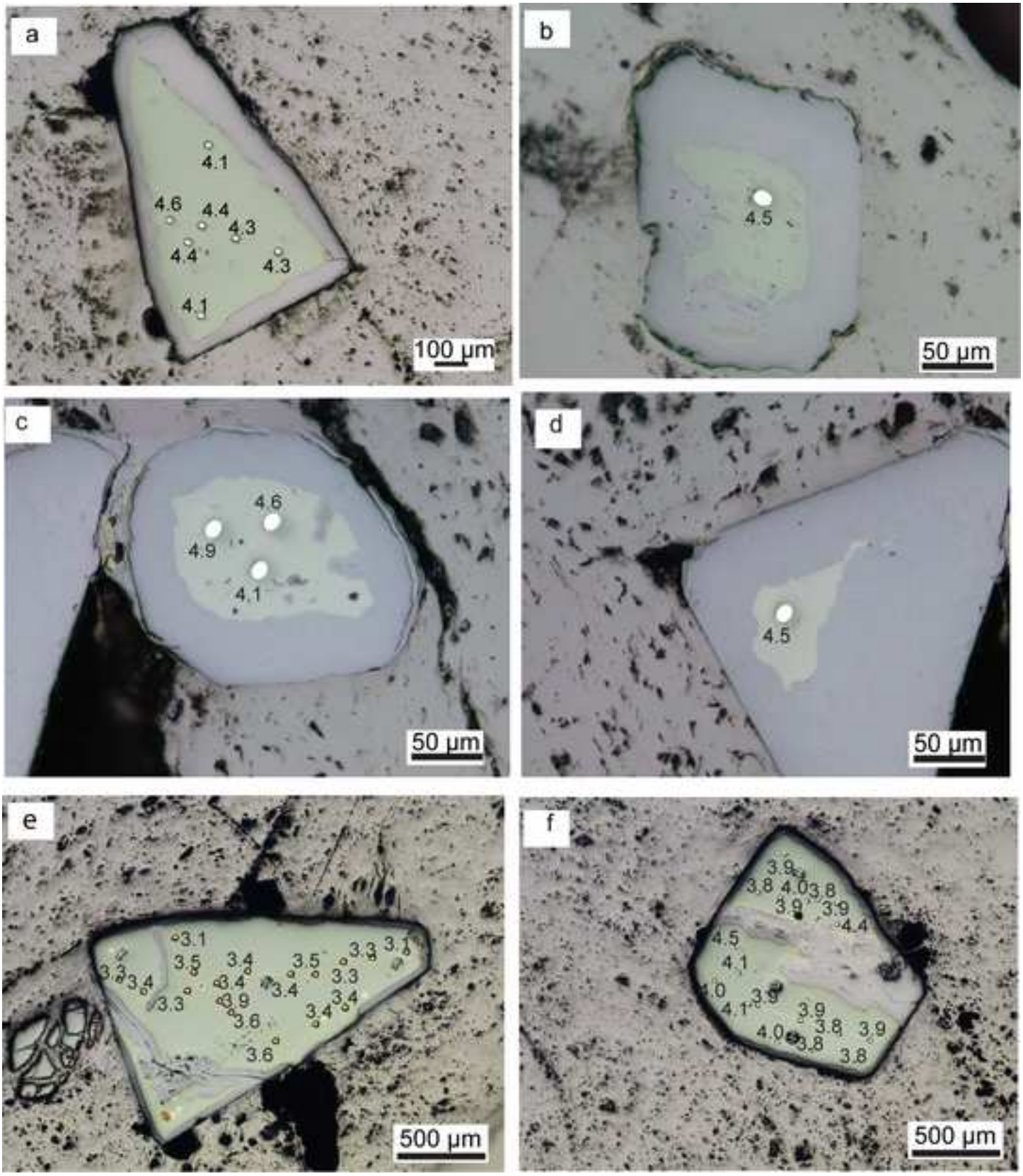

Figure 10

Click here to download high resolution image

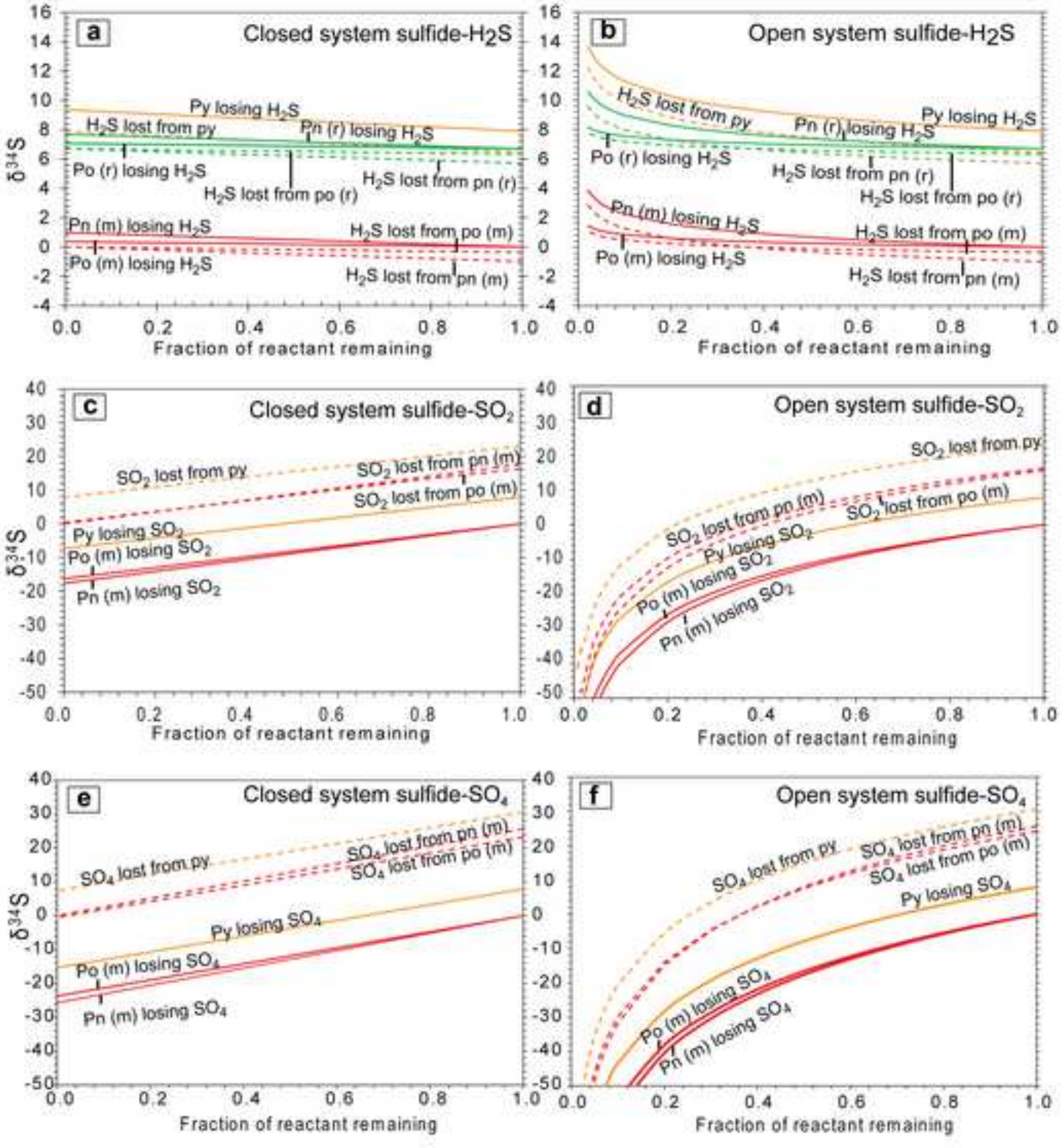

Figure 11

Click here to download high resolution image

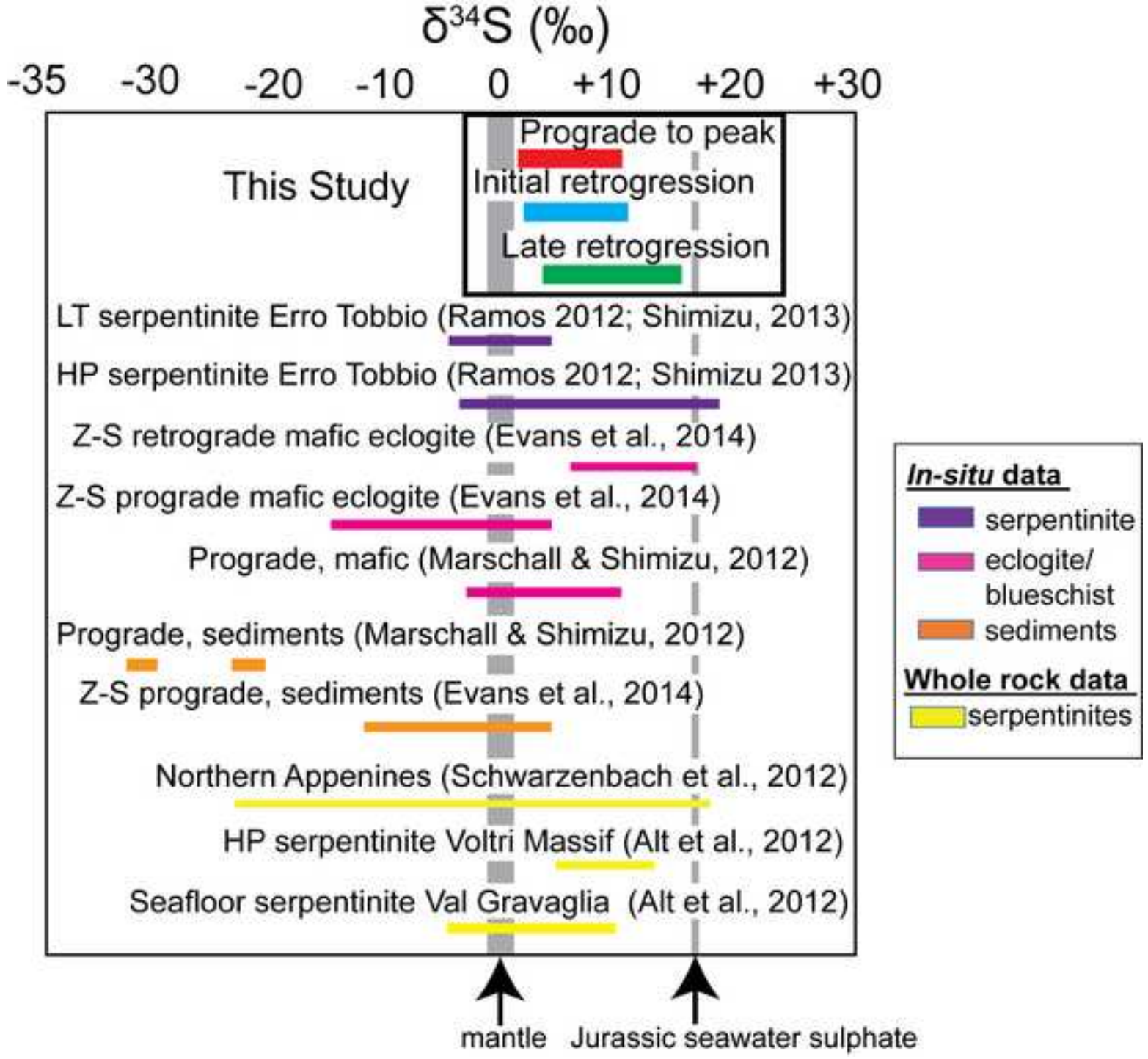

Table 1
Click here to download Table: Table 1.docx

Table 1: EPMA data for sulfides. Number in brackets is two standard deviations. b.d.l indicates the concentration is below detection

Sample	CO13-40	CO13-33	CO13-33	CO13-33	CO13-55	CO13-55	CO13-55	CO14-03	CO14-04	CO14-04
Phase	Pn1 (n=10)	Pn1 (n=6)	Pn2(n=14)	Pn3(n=10)	Pn1(n=9)	Pn2(n=8)	Pn3(n=13)	Py3(n=38)	Py1(n=21)	Py2(n=31)
wt%										
Si	n.d.	0.02(1)	0.04(3)	0.03(1)	0.05(3)	0.1(1)	0.04(4)	b.d.l	b.d.l	b.d.l
Mg	n.d.	0.09(9)	0.10(9)	0.05(4)	0.08(7)	0.07(4)	0.06(3)	b.d.l	b.d.l	b.d.l
Ni	34(2)	37.2(4)	37.1(3)	37.2(5)	37.5(8)	36(2)	37(1)	b.d.l	0.2(2)	0.2(2)
Fe	28.4(7)	25.3(4)	26.6(3)	26.1(5)	25.5(9)	26(1)	26(2)	45.3(5)	46.8(2)	46.8(4)
Co	1.8(2)	2.40(6)	2.32(5)	2.37(8)	2.3(2)	2.2(2)	2.3(2)	1.0(4)	0.1(3)	0.1(3)
S	35(2)	33.1(5)	33.3(3)	33.2(4)	33.4(2)	33.2(5)	33.3(2)	53.3(2)	53.9(3)	53.9(3)
Cu	n.d.	0.01(1)	0.1(2)	0.01(1)	0.01(1)	0.010(3)	0.01(1)	b.d.l	b.d.l	b.d.l
Se	n.d.	0.15(1)	0.01(1)	0.14(2)	0.16(1)	0.16(1)	0.15(2)	n.d.	n.d.	n.d.
Bi	n.d.	0.12(1)	0.13(1)	0.13(1)	0.13(1)	0.120(4)	0.13(1)	n.d.	n.d.	n.d.
As	n.d.	0.24(1)	0.22(2)	0.23(1)	0.27(4)	0.27(2)	0.25(3)	b.d.l	b.d.l	b.d.l
Sb	n.d.	0.02(1)	0.01(1)	0.01(1)	0.02(1)	0.02(2)	0.02(1)	0.02(1)	0.02(1)	0.01(1)
TOTAL	98.9(7)	99(1)	99.2(5)	99.7(5)	99.5(7)	98.6(7)	98.7(5)	100.4(3)	101.1(3)	101.1(3)
mol%										
Ni	26.9(8)	29.27(7)	29.1(2)	29.1(3)	29.3(6)	28(1)	29(1)	-	0.1(1)	0.1(1)
Fe	23.3(6)	21.0(2)	21.1(2)	21.4(5)	20.9(7)	22(1)	21(1)	32.5(3)	33.2(1)	33.2(3)
Co	1.3	1.88(5)	1.81(4)	1.85(6)	1.8(1)	1.7(1)	1.8(2)	0.7(3)	0.1(2)	0.1(1)
S	49(1)	47.8(2)	47.9(2)	47.5(3)	47.8(2)	47.9(3)	47.9(2)	66.79(9)	66.6(2)	66.6(2)
S/Fe+Ni+Co	0.94(5)	0.92(1)	0.92(1)	0.91(1)	0.92(1)	0.92(1)	0.92(1)	2.011(8)	2.2(2)	2.2(3)

Table 2
Click here to download Table: Table 2.docx

Table 1: Average $\delta^{34}S$ sulfur isotope analyses of individual pentlandite (pn) and pyrite (py) grains. 'Stage' corresponds to the metamorphic stage of the sulphide grain growth; P = prograde to peak metamorphism, EE = Early Exhumation, LE = Late Exhumation. The full analytical results are reported in Appendix B. N.a. = not applicable for single analyses of grains.

Grain	Sulfide	Average $\delta^{34}S_{VCDT}$ (‰)	External 2σ (‰)	# Analyses	Av 2σ on single grain (‰)	Stage
CO13-40						
CO13-40-a1-s1	Pn1	7.23	1.22	3	0.98	P
CO13-40-a1-s2	Pn1	9.33	2.33	2	1.03	P
CO13-40-a1-s3	Pn1	8.80	n.a.	1	0.93	P
CO13-40-a1-s4	Pn1	4.27	n.a.	1	1.10	P
CO13-40-a2-s1	Pn1	7.57	n.a.	1	0.31	P
CO13-40-a2-s2	Pn1	5.39	n.a.	1	0.37	P
CO13-40-a2-s3	Pn1	6.32	0.35	2	0.46	P
CO13-40-a3-s1	Pn1	6.72	1.04	3	0.36	P
CO13-40-a3-s2	Pn1	5.93	0.99	2	0.46	P
CO13-40-a3-s3	Pn1	8.85	n.a.	1	0.32	P
CO13-40-a3-s4	Pn1	10.43	n.a.	1	0.90	P
CO13-40-a3-s5	Pn1	6.77	n.a.	1	1.14	P
CO13-40-a3-s6	Pn1	6.21	n.a.	1	1.09	P
CO13-40-a3-s8	Pn1	8.73	2.15	3	0.96	P
CO13-40-a3-s9	Pn1	8.81	0.04	2	0.81	P
CO13-40-a3-s10	Pn1	9.36	n.a.	1	0.86	P
CO13-40-a3-13	Pn1	8.83	n.a.	1	0.78	P
CO13-40-a3-14	Pn1	5.03	n.a.	1	0.79	P
CO13-40-a3-15	Pn1	4.39	n.a.	1	0.94	P
CO13-40-a3-16	Pn1	8.03	n.a.	1	0.82	P
CO13-33						
CO13-33-a2-s2	Pn2	5.50	n.a.	1	0.76	EE
CO13-33-a2-s3	Pn2	7.88	n.a.	1	0.74	EE
CO13-33-a2-s4	Pn2	9.19	0.81	2	0.81	EE
CO13-33-a2-s5	Pn3	3.89	n.a.	1	0.90	LE
CO13-33-a2-s6	Pn3	7.27	n.a.	1	0.75	LE
CO13-33-a2-s7	Pn3	8.42	n.a.	1	0.72	LE
CO13-33-a2-s8	Pn3	8.20	n.a.	1	0.82	LE
CO13-33-a2-s9	Pn2	7.91	n.a.	1	0.76	EE
CO13-33-a3-s1	Pn1	5.47	n.a.	1	0.78	P
CO13-33-a3-s2	Pn1	8.82	n.a.	1	0.79	P
CO13-33-a3-s4	Pn2	6.54	n.a.	1	0.73	EE
CO13-33-a3-s6	Pn2	7.54	n.a.	1	0.83	EE
CO13-33-a3-s7	Pn2	7.56	n.a.	1	0.74	EE
CO13-33-a3-s10	Pn3	1.75	n.a.	1	0.74	LE
CO13-33-a3-s13	Pn1	6.53	n.a.	1	0.74	P
CO13-33-a3-s14	Pn1	8.40	n.a.	1	0.75	P
CO13-33-a3-s15	Pn2	7.78	n.a.	1	0.76	EE
CO13-55						
CO13-55-a1-s1	Pn3	6.02	0.75	2	0.35	LE
CO13-55-a1-s2	Pn1	5.18	1.66	2	0.36	P
CO13-55-a1-s3	Pn3	5.91	n.a.	1	0.42	LE
CO13-55-a2-s1	Pn1	4.97	0.83	4	0.41	P
CO13-55-a2-s2	Pn2	3.25	0.20	2	0.38	EE
CO13-55-a2-s3	Pn2	5.90	0.82	2	0.39	EE
CO13-55-a3-s1	Pn3	7.44	0.36	2	0.36	LE
CO13-55-a3-s2	Pn1	3.13	0.22	3	0.41	P
CO13-55-a3-s2b	Pn1	2.95	n.a.	1	0.50	P
CO14-03						
CO14-03-a1-1-8	Py3	6.85	0.58	9	0.21	LE
CO14-03-a2-1-4	Py3	12.70	1.99	4	0.21	LE
CO14-03-a2-5	Py3	15.08	n.a.	1	0.21	LE
CO14-03-a2-7-8	Py3	10.30	3.93	2	0.21	LE
CO14-03-a2-9-13	Py3	8.13	1.75	5	0.21	LE
CO14-03-a3-1-2	Py3	7.79	0.29	2	0.21	LE
CO14-03-a3-3-4	Py3	11.16	3.14	2	0.21	LE
CO14-03-a3-5-6	Py3	10.54	4.20	2	0.21	LE
CO14-03-a3-7-8	Py3	7.32	0.37	2	0.21	LE
CO14-03-a3-9-11	Py3	10.17	3.26	3	0.22	LE
CO14-04						

CO14-04-a1-s1	Py2	3.96	0.20	17	0.15	EE
CO14-04-a2-s1, 1-9, 22-32	Py2	4.48	0.22	20	0.11	EE
CO14-04-a2-s2, 11-14, 21-23	Py1	4.31	0.16	7	0.11	P
CO14-04-a2-s3	Py1	5.06	0.10	1	0.10	P
CO14-04-a3-s1	Py1	5.06	0.40	3	0.10	P
CO14-04-a3-s2	Py1	5.02	n.a.	1	0.10	P

Table 3
Click here to download Table: Table 3.docx

Table 1: non zero $\Delta^{33}S$ sulfur isotope analyses in pentlandite (pn) and pyrite (py) grains.

Grain	Sulfide	$\Delta^{33}S_{VCDT}$ (‰)	2σ abs (‰)
CO13-40			
CO13-40 a3 s1-2	Pn1	0.52	0.30
CO13-40 a3 s3	Pn1	0.38	0.24
CO13-40 a3 s12-3	Pn1	0.67	0.50
CO13-55			
CO13-55 a2 s1-1	Pn1	0.33	0.23
CO13-55 a2 s3-1	Pn2	0.37	0.28
CO13-55 a3 s2-1	Pn1	0.38	0.23
CO13-55 a3 s2-4	Pn1	0.49	0.31
CO14-04			
CO14-04 s1 a1	Py1	0.11	0.10
CO14-04 s1 a2	Py2	-0.16	0.12
CO14-04 s1 a3	Py1	-0.17	0.15

Appendix A

Click here to download Background dataset for online publication only: Appendix_A_S_isotope_data_reduction.pdf

Appendix B

Click here to download Background dataset for online publication only: Appendix_B_sulfide_compositions_.xlsx

Appendix C

Click here to download Background dataset for online publication only: Appendix_C_S_isotope_compositions.docx

Appendix D

Click here to download Background dataset for online publication only: Appendix_D_Mann_Whitney_U_test.pdf